



# Group Velocity–Driven Inverse Metamaterial Design

Heedong Goh, S.M.ASCE<sup>1</sup>; and Loukas F. Kallivokas, M.ASCE<sup>2</sup>

**Abstract:** We are concerned with controlling wave propagation in an elastic medium by engineering its dispersive properties. To this end, we discuss a flexible and systematic framework for designing the material composition of the unit cell of a periodic medium when given a target dispersion relation or, equivalently, a target group velocity profile at a user-defined frequency range. We cast the inverse medium design problem as a dispersion-constrained optimization problem that minimizes the distance between the target and the computed group velocity profiles. We rely on the Hellmann–Feynman theorem to obtain the computed group velocity of a trial unit cell, and use a gradient-based algorithm to drive the engineered medium’s material properties to convergence. We numerically demonstrate the capabilities of the approach using scalar waves in one and two dimensions. We also use the method to design metamaterials exhibiting user-defined omnidirectional band gaps and to provide numerical evidence of the metamaterial’s intended performance via time-domain simulations. DOI: 10.1061/(ASCE)EM.1943-7889.0001688. © 2019 American Society of Civil Engineers.

**Author keywords:** Dispersion engineering; Inverse metamaterial design; Group velocity; band gap.

## Introduction

The interest in understanding and modeling wave propagation in periodic structures is centuries old, originating possibly with the modeling of spring-mass chains; important contributions can be found in the seminal works of Newton (1740), Rayleigh (1887), and Brillouin (1946). Recent renewed attention to waves in periodic structures is due to the ability to design and manufacture periodic media at various length scales that exhibit unconventional properties (Movchan et al. 2018), which, in turn, can be harnessed to advantage. Whereas the periodic structure’s unit cell constituent materials have conventional properties (e.g., positive mass density and positive elastic modulus) the composite periodic structure’s homogenized properties may exhibit singly negative, or doubly negative material properties, thus endowing the structure with metamaterial status.

The exotic or unconventional properties of metamaterials are exploited to drive novel applications in solid state physics, in photonics, and in phononics; related contributions of note include the works of Pendry (2000) and Luo et al. (2003) in subwavelength focusing, and of Alù and Engheta (2005), Schurig et al. (2006), Norris (2008), and Brun et al. (2009) in invisibility cloaking. The aforementioned, as well as similar developments in optics have fueled interest in extending the gains realized therein to the case of media supporting elastic waves, most notably for seismic shielding applications (Meseguer et al. 1999; Alagoz and Alagoz 2011; Krödel et al. 2015; Miniaci et al. 2016; Colombi et al. 2016a; Palermo et al. 2018), despite the difficulties imposed by the presence of two different bulk wave types and large wavelengths.

Whether in optics or elastodynamics, key interests include the design of metamaterials capable of steering or channeling waves, band-gapping, filtering, focusing, etc. (Dubois et al. 2013; Finocchio et al. 2014; Torrent et al. 2014; Climente et al. 2014; Colombi 2016; Colombi et al. 2016b; Huang et al. 2017). Irrespective of the application field, to date, metamaterial design is done on an ad hoc basis, driven mostly by physical insight: no systematic process has been proposed to guide either the topological or material inverse problems associated with the design of a metamaterial when given a target outcome. Examples of a few exceptions include band-gap maximization (Sigmund and Søndergaard Jensen 2003; Qian and Sigmund 2011), wave amplitude control (Rupp et al. 2007; Biros et al. 2004), design for effective medium properties (Wang et al. 2014), a topological optimization for optical waveguides (Castelló-Lurbe et al. 2014), optimal design of seismic metamaterials (Wagner et al. 2018), and the systematic approach for metamaterial band gap design in Goh and Kallivokas (2019).

Specifically, in Goh and Kallivokas (2019), we proposed a method for designing a metamaterial exhibiting a user-defined band gap, using the discriminant of the associated quadratic eigenvalue problem as the inverse medium problem driver. Though systematic, the approach is limited to band gaps: broader design considerations, including wave directivity control, spectrum-specific wave speed control, multiple target band gaps, etc., can only be accommodated if the design approach considers the dispersive behavior in a holistic manner. Thus, to design the topology or the material properties of a metamaterial in order for it to exhibit a user-prescribed behavior, requires engineering the metamaterial’s dispersive characteristics, or, equivalently, its dispersion curve(s)/surface(s). A suitable metric—perhaps the most suitable—for engineering the dispersion curve is its *derivative*, i.e., the group velocity, for it readily allows for the simultaneous consideration of several of the aforementioned design targets.

It is noted that engineering the dispersion curve(s), or equivalently the group velocity profile, is a bona fide inverse medium problem. In this article, we describe a systematic method for designing a metamaterial unit cell to exhibit a user-defined group velocity profile. The associated inverse medium problem borrows from the systematic framework used in related work in inverse medium geoscience problems (Kallivokas et al. 2013; Fathi et al. 2015; Mashayekh et al. 2018; Kucukcoban et al. 2019).

<sup>1</sup>Graduate Student, Dept. of Civil, Architectural, and Environmental Engineering, Univ. of Texas at Austin, Austin, TX 78712. ORCID: <https://orcid.org/0000-0003-4854-6435>

<sup>2</sup>Professor, Oden Institute for Computational Engineering and Sciences, Univ. of Texas at Austin, Austin, TX 78712 (corresponding author). ORCID: <https://orcid.org/0000-0002-7701-6989>. Email: [loukas@mail.utexas.edu](mailto:loukas@mail.utexas.edu)

Note. This manuscript was submitted on November 25, 2018; approved on April 24, 2019; published online on September 19, 2019. Discussion period open until February 19, 2020; separate discussions must be submitted for individual papers. This paper is part of the *Journal of Engineering Mechanics*, © ASCE, ISSN 0733-9399.

The structure of the article is as follows: we briefly review the dispersive characteristics of a periodic medium and discuss the complex band structure, band gaps, and group velocity. Then, we define the metamaterial unit cell design problem driven by a target group velocity profile, and describe the resolution of the associated inverse medium problem. Numerical examples resulting in the design of one- and two-dimensional unit cells are provided to demonstrate the method's capabilities in the frequency domain, including the design of a unit cell exhibiting an omnidirectional user-defined band gap. Lastly, we reinforce the findings via time-domain simulations, with limited-width metamaterial blocks that show sub-wavelength performance.

## Preliminaries

We are interested in controlling a medium's dispersive properties. To fix ideas, we use a target group velocity profile to drive the inverse metamaterial design problem. Band gaps and other similar design goals emerge as particular cases of the group velocity design problem. To describe the approach, we appeal first to the properties of the eigenvalue problem of a periodic medium.

### Periodic Medium and Its Complex Dispersion Relation

A periodic medium is characterized by a dispersion relation exhibiting band gaps, backward propagating waves, slow and fast waves, mode conversions, etc. To arrive at the dispersion relation of a periodic medium, we begin with a quadratic eigenvalue problem. To this end, consider the scalar Helmholtz equation in  $N_d$ -dimensional space, i.e.

$$0 = \operatorname{div}[\mu(\mathbf{x})\operatorname{grad}U(\mathbf{x})] + \rho(\mathbf{x})\omega^2U(\mathbf{x}), \quad \mathbf{x} \in \mathbb{R}^{N_d} \quad (1)$$

where, for a scalar elastodynamic problem,  $U(\mathbf{x})$  = displacement;  $\mu(\mathbf{x})$  = shear modulus;  $\rho(\mathbf{x})$  = density; and  $\omega$  = temporal frequency. For a periodic medium, the spatial distribution of the material properties satisfy

$$\rho(\mathbf{x}) = \rho\left(\mathbf{x} + \sum_{i=1}^{N_d} m_i \mathbf{p}_i\right) \quad \text{and} \quad (2a)$$

$$\mu(\mathbf{x}) = \mu\left(\mathbf{x} + \sum_{i=1}^{N_d} m_i \mathbf{p}_i\right) \quad \forall \mathbf{x} \in \mathbb{R}^{N_d}, \quad \forall m_i \in \mathbb{Z} \quad (2b)$$

Each primitive vector  $\mathbf{p}_i \in \mathbb{R}^{N_d}$  defines the periodicity in the  $i$ th direction, and  $m_i$  is an arbitrary integer. For example, a choice of  $\mathbf{p}_1 = (1, 0)$  and  $\mathbf{p}_2 = (0, 1)$  defines a square periodic unit cell in a two-dimensional plane. Then, the Bloch theorem (Ashcroft 1976) provides the general solution of Eq. (1) under the periodicity relations of Eq. (2), as

$$U(\mathbf{x}) = e^{i\mathbf{k}\cdot\mathbf{x}}u(\mathbf{x}) \quad (3)$$

where the displacement-like quantity  $u(\mathbf{x})$  is also periodic with the same periodicity  $\mathbf{p}_i$  of the medium, and  $\mathbf{k}$  is the Bloch wavevector. Thus, the general solution  $U(\mathbf{x})$  consists of a plane wave  $e^{i\mathbf{k}\cdot\mathbf{x}}$  enveloped by the periodic function  $u(\mathbf{x})$ . The Bloch theorem allows us to obtain an eigenvalue problem defined over a unit cell  $\Omega_{\text{cell}}$  by substituting the general solution of Eq. (3) into the Helmholtz Eq. (1). Then, in weak form, the eigenvalue problem can be cast as (Banerjee 2011)

$$0 = \int_{\Omega_{\text{cell}}} [(-ik\mathbf{d}\bar{v} + \operatorname{grad}\bar{v}) \cdot \mu(i\mathbf{k}\mathbf{d}u + \operatorname{grad}u) - \bar{v}\rho\omega^2u]d\Omega \quad (4)$$

In Eq. (4),  $k = \mathbf{k} \cdot \mathbf{d}$  is the wavevector in any direction of interest  $\mathbf{d}$ ,  $v$  is a test function, and an overline ( $\bar{\cdot}$ ) denotes complex conjugation of the subtended quantity. For a given real-valued  $\omega$ , the eigenvalue problem in Eq. (4) can be solved for a complex-valued  $k$ . Specifically, we rearrange the weak form of Eq. (4) to obtain the following quadratic eigenvalue problem:

Given  $\omega \in \mathbb{R}$  and  $\mathbf{d} \in \mathbb{R}^{N_d}$ , find  $k \in \mathbb{C}$  and  $u \in \mathcal{V} \setminus \{0\}$  such that

$$0 = a_0(v, u) + ka_1(v, u) + k^2a_2(v, u) \equiv P(k)(u, v) \quad \forall v \in \mathcal{V} \quad (5)$$

where

$$\mathcal{V} = \left\{ u \in H^1(\Omega_{\text{cell}}) \mid u(\mathbf{x}) = u\left(\mathbf{x} + \sum_{i=1}^{N_d} m_i \mathbf{p}_i\right) \quad \forall \mathbf{x} \in \partial\Omega_{\text{cell}} \right\} \quad (6a)$$

$$a_0(v, u) = \int_{\Omega_{\text{cell}}} [\operatorname{grad}\bar{v} \cdot \mu\operatorname{grad}u - \bar{v}\omega^2\rho u]d\Omega \quad (6b)$$

$$a_1(v, u) = i \int_{\Omega_{\text{cell}}} [\operatorname{grad}\bar{v} \cdot \mu\mathbf{d}u - \mathbf{d}\bar{v} \cdot \mu\operatorname{grad}u]d\Omega, \quad \text{and} \quad (6c)$$

$$a_2(v, u) = \int_{\Omega_{\text{cell}}} \mathbf{d}\bar{v} \cdot \mu\mathbf{d}u d\Omega \quad (6d)$$

Notice that the dispersion relation is symmetric about  $\mathbf{k} = \mathbf{0}$ , and periodic with periodicity of  $2\pi\mathbf{q}_i$ . Moreover,  $\mathbf{q}_i$  are the reciprocal primitive vectors satisfying  $\mathbf{p}_i \cdot \mathbf{q}_j = 2\pi\delta_{ij}$ , where  $\delta_{ij}$  is a Kronecker delta. The complete dispersion relation, or equivalently, the band structure is the collection of dispersion curves obtained from solving Eq. (5).

We note that the quadratic eigenvalue problem of Eq. (5) is also characterized by a discriminant  $\mathcal{D}$ , which allows distinguishing between propagating and nonpropagating states (Goh and Kallivokas 2019). Specifically, by replacing the test function  $v$  with  $u$  in Eq. (5), we obtain

$$\begin{aligned} 0 &= P(k)(u, u) \\ &= a_0(u, u) + ka_1(u, u) + k^2a_2(u, u) \\ &= c + bk + ak^2 \end{aligned} \quad (7)$$

where  $a$ ,  $b$ , and  $c$  are real-valued scalars due to the Hermitian character of  $a_i(\cdot, \cdot)$ . Then, the discriminant of the quadratic Eq. (7) is given by

$$\mathcal{D} = b^2 - 4ac \quad (8)$$

A positive  $\mathcal{D}$  implies a propagating state, or a real-valued  $k$ , and a negative  $\mathcal{D}$  implies a nonpropagating state, or a complex-valued  $k$ . If the sole aim of the unit cell design is to engineer the periodic structure to exhibit user-defined band gaps, the design problem can be driven by the discriminant, as was done in Goh and Kallivokas (2019). If, however, broader design goals are of interest, e.g., a target slow-wave region, lensing, or focusing, then relying on the discriminant alone is not sufficient. The more general problem of engineering the dispersive properties requires consideration of the

group velocity: in the next section, we relate the group velocity to the parameters of the eigenvalue problem in Eq. (5).

### Group Velocity in Terms of the Eigenpair

The group velocity  $\mathbf{v}_g$  is defined as the real part of the complex group velocity (Moiseyenko and Laude 2011), i.e.

$$\mathbf{v}_g = \text{Re}\{\text{grad}_k \omega\} = \sum_{i=1}^{N_d} \text{Re}\left\{\frac{\partial \omega}{\partial k_i}\right\} \mathbf{e}_i \quad (9)$$

where  $\mathbf{e}_i$  are orthonormal bases. Substituting  $v$  with  $u$ , and taking a partial derivative of Eq. (5) with respect to  $k$ , results in

$$\begin{aligned} 0 &= \frac{\partial}{\partial k} P(k)(u, u) \\ &= 2\omega \frac{\partial \omega}{\partial k} a_{0,2}(u, u) + a_1(u, u) + 2ka_2(u, u) \\ &\quad + 2\text{Re}\left\{a_{0,0}\left(\frac{\partial u}{\partial k}, u\right)\right\} + 2\omega^2 \text{Re}\left\{a_{0,2}\left(\frac{\partial u}{\partial k}, u\right)\right\} \\ &\quad + 2k \text{Re}\left\{a_1\left(\frac{\partial u}{\partial k}, u\right)\right\} + 2k^2 \text{Re}\left\{a_2\left(\frac{\partial u}{\partial k}, u\right)\right\} \end{aligned} \quad (10)$$

In deriving Eq. (10), we decomposed  $a_0(v, u)$  into two parts: a term with no  $\omega$ -dependency, denoted by  $a_{0,0}(v, u)$ , and a term exhibiting  $\omega^2$ -dependency, denoted by  $\omega^2 a_{0,2}(v, u)$ , i.e.

$$a_0(v, u) = a_{0,0}(v, u) + \omega^2 a_{0,2}(v, u) \quad (11)$$

Taking the real part of Eq. (10), results in

$$\begin{aligned} 0 &= 2\omega \text{Re}\left\{\frac{\partial \omega}{\partial k}\right\} a_{0,2}(u, u) + a_1(u, u) + 2\text{Re}\{k\} a_2(u, u) \\ &\quad + 2\text{Re}\left\{a_{0,0}\left(\frac{\partial u}{\partial k}, u\right) + \omega^2 a_{0,2}\left(\frac{\partial u}{\partial k}, u\right)\right\} \\ &\quad + ka_1\left(\frac{\partial u}{\partial k}, u\right) + k^2 a_2\left(\frac{\partial u}{\partial k}, u\right) \end{aligned} \quad (12)$$

Assuming  $\partial u / \partial k \in \mathcal{V}$ , the terms involving  $\partial u / \partial k$  in Eq. (12) vanish because  $u$  is the eigenvector satisfying Eq. (5). Then, the group velocity in the direction  $\mathbf{d}$ , or  $\mathbf{v}_g \cdot \mathbf{d}$ , is written in terms of the eigenpair  $(u, k)$  as

$$\begin{aligned} v_g &= \mathbf{v}_g \cdot \mathbf{d} \\ &= \text{Re}\left\{\frac{\partial \omega}{\partial k}\right\} = \text{Re}\left\{-\frac{a_1(u, u) + 2ka_2(u, u)}{2\omega a_{0,2}(u, u)}\right\} \\ &= -\frac{a_1(u, u) + 2\text{Re}\{k\} a_2(u, u)}{2\omega a_{0,2}(u, u)} \end{aligned} \quad (13)$$

Eq. (13) can be regarded as the (scalar) elastodynamic equivalent of the Hellmann–Feynman theorem in quantum mechanics, which relates the derivative of the total energy to the derivative of the associated Hamiltonian. A similar approach for computing the group velocity in optics is reported in Sakoda (2004).

As it can be seen from Eq. (13), the group velocity in a given direction  $\mathbf{d}$  is expressed explicitly in terms of the eigenvectors and eigenvalues of the associated eigenvalue problem. Thus, engineering the dispersive properties of a unit cell to achieve a user-defined wave control outcome is equivalent to prescribing the group

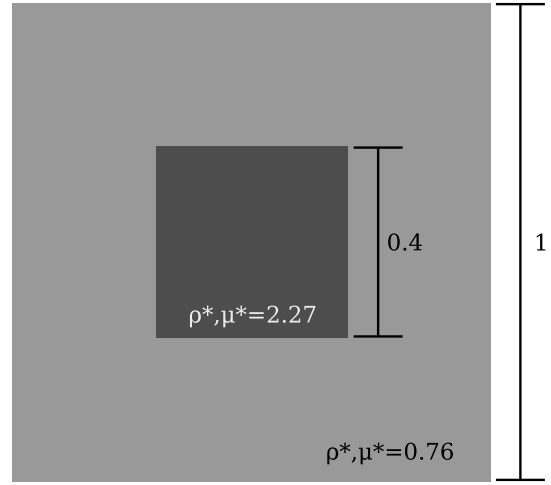


Fig. 1. Square unit cell prototype.

velocity along user-defined directions  $\mathbf{d}$ . Wave-steering, lensing, focusing, band gaps, etc., can all be cast in terms of a target group velocity profile (along one or multiple directions). For example, designing for a user-defined band gap requires that the target group velocity, for a set of desired directions, vanish, i.e.

$$v_g = \mathbf{v}_g \cdot \mathbf{d} = -\frac{a_1(u, u) + 2\text{Re}\{k\} a_2(u, u)}{2\omega a_{0,2}(u, u)} = 0 \quad (14)$$

We note that the band-gap criterion  $\mathcal{D} < 0$  established in Goh and Kallivokas (2019) is equivalent to prescribing a zero group velocity (see Appendix I for proof).

We capture schematically the preceding discussion by considering the square unit cell depicted in Fig. 1, composed of two concentric square zones of piecewise constant material properties written in terms of nondimensionalized quantities

$$\begin{aligned} u^* &= \frac{u}{p}, & \rho^* &= \frac{\rho}{\rho_{\text{avg}}}, & \mu^* &= \frac{\mu}{\mu_{\text{avg}}}, \\ x^* &= \frac{x}{p}, & \omega^* &= \frac{\omega p}{c_{\text{avg}}}, & \text{and } k^* &= kp \end{aligned} \quad (15)$$

where  $p = \max|\mathbf{p}_i|$  and  $(\cdot)_{\text{avg}}$  is used for area-averaged quantities. The average wave speed  $c_{\text{avg}}$  is computed by  $\sqrt{\mu_{\text{avg}}/\rho_{\text{avg}}}$ . Then, Figs. 2(a and b) show the dispersion relation in terms of the complex band structure. In Fig. 2(a), hollow gray circles are used to denote the real part of the complex-valued  $k^*$ , whereas black dots are used for real-valued  $k^*$ . Because of the symmetry and periodicity of the dispersion relation, the band structure is provided only along the high symmetry lines  $\Gamma - X$ ,  $\Gamma - M$ , and  $X - M$ , which circumscribe the irreducible Brillouin zone. The shaded zone shown in Fig. 2(a) corresponds to an omnidirectional band gap in the range  $\omega^* \in (3.3, 3.6)$ . Fig. 2(b) shows the imaginary part of the band structure: notice that the region corresponding to nonzero  $\text{Im}\{k^*\}$  represents the band gap. Similarly, Fig. 2(c) shows the discriminant  $\mathcal{D}$  distribution: notice that the range of  $\omega^*$  for which  $\mathcal{D} < 0$  identifies uniquely the band gap. Lastly, Fig. 2(d) shows the group velocity, where clearly the zone where the velocity vanishes delineates the same band gap identified in Figs. 2(a–c): for band gaps, all four representations shown in Fig. 2 are equivalent.

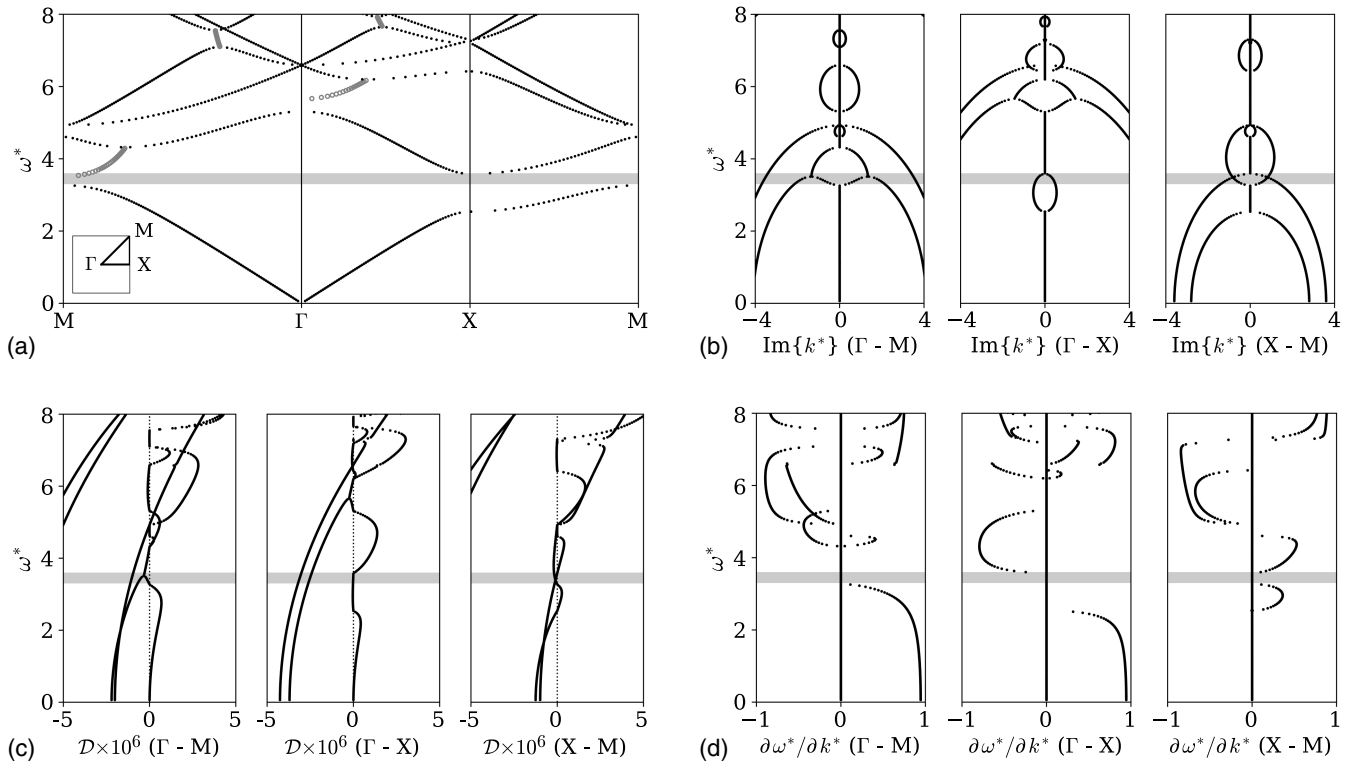


**Fig. 2.** Complex band structure, discriminant, and group velocity: an omnidirectional band gap is shown shaded in the range  $\omega^* \in (3.3, 3.6)$ : (a) real part of the band structure: real-valued  $k^*$  are shown as dots, whereas hollow circles are used for complex-valued  $k^*$ ; (b) imaginary part of the band structure: nonpropagating states (band gap) have nonzero imaginary part; (c) discriminant  $\mathcal{D}$  distribution: nonpropagating states (band gap) correspond to negative  $\mathcal{D}$  values; and (d) group velocity: nonpropagating states (band gap) correspond to zero  $v_g$ .

### Group Velocity Control

In this section, we introduce the inverse problem and its solution method for designing a unit cell of a periodic medium when a target group velocity profile is given. We begin by defining the objective functional and the optimality conditions, where the inverse design problem is cast as a minimization problem. Then, we introduce a gradient-based inversion process to iteratively update the trial design variables  $\rho$  and  $\mu$  to converge to the optimum. The design variables depend on the desirable parameterization of the unit cell, e.g., they can be material properties when the topology is fixed,

or topological parameters when material properties are fixed, etc. Herein, we choose material properties  $\rho$  and  $\mu$  as design variables, for a fixed unit cell topology.

### Objective Functional

We use a misfit functional to drive the inverse medium problem. The misfit functional  $M$  is defined using the distance between the computed group velocities of a trial unit cell and the prescribed target group velocities at different temporal frequencies, modes, and directions, i.e.

$$\begin{aligned}
 M[\rho, \mu, u_{\alpha, \beta, \gamma}, k_{\alpha, \beta, \gamma}] &= \sum_{\alpha}^{N_{\text{freq}}} \sum_{\beta}^{N_{\text{dir}}} \sum_{\gamma}^{N_{\text{mode}}} \frac{1}{2} [(\mathbf{v}_g)_{\alpha, \gamma} \cdot \mathbf{d}_{\beta} - (v_g^m)_{\alpha, \beta, \gamma}]^2 \\
 &= \sum_{\alpha}^{N_{\text{freq}}} \sum_{\beta}^{N_{\text{dir}}} \sum_{\gamma}^{N_{\text{mode}}} \frac{1}{2} \left[ \text{Re} \left\{ -\frac{a_1(u_{\alpha, \beta, \gamma}, u_{\alpha, \beta, \gamma}) + 2k_{\alpha, \beta, \gamma} a_2(u_{\alpha, \beta, \gamma}, u_{\alpha, \beta, \gamma})}{2\omega_{\alpha} a_{0,2}(u_{\alpha, \beta, \gamma}, u_{\alpha, \beta, \gamma})} \right\} - (v_g^m)_{\alpha, \beta, \gamma} \right]^2
 \end{aligned} \tag{16}$$

where  $N_{\text{freq}}$ ,  $N_{\text{dir}}$ , and  $N_{\text{mode}}$  denote the number of frequencies, directions, and modes, respectively, over which the target group velocity  $(v_g^m)_{\alpha, \beta, \gamma}$  is defined. Indices  $\alpha$ ,  $\beta$ , and  $\gamma$ , are used to denote the individual frequency, direction, and mode, respectively; to reduce notational congestion, we henceforth omit the subscripts, i.e.

$$v_g^m = (v_g^m)_{\alpha, \beta, \gamma}, \quad \mathbf{v}_g = (\mathbf{v}_g)_{\alpha, \gamma}, \quad \mathbf{d} = \mathbf{d}_{\beta}, \quad u = u_{\alpha, \beta, \gamma}, \quad k = k_{\alpha, \beta, \gamma}, \quad \text{and} \quad \omega = \omega_{\alpha} \tag{17}$$

We note that, should a band gap be a design target, then  $v_g^m$  should be set to zero.

Next, we augment the misfit functional  $M$  by side-imposing the dispersion relation using Lagrangian multipliers, i.e., let

$$L[\rho, \mu, u, k, v, \xi] = M[\rho, \mu, u, k] + E[\rho, \mu, u, k, v, \xi] \tag{18}$$

where  $L$  denotes the unit cell's Lagrangian, and  $E$  is the associated eigenvalue problem constraint defined as

$$E[\rho, \mu, u, k, v, \xi] = \sum_{\alpha}^{N_{\text{freq}}} \sum_{\beta}^{N_{\text{dir}}} \sum_{\gamma}^{N_{\text{mode}}} \text{Re}\{P(k)(v, u)\} + \sum_{\alpha}^{N_{\text{freq}}} \sum_{\beta}^{N_{\text{dir}}} \sum_{\gamma}^{N_{\text{mode}}} \frac{\xi}{2} [a_2(u, u) - 1] \quad (19)$$

In Eq. (19), the first term is the eigenvalue problem, whereas the second term is the side-imposition of the orthonormality condition that ensures a unique set of eigenvectors;  $v$  and  $\xi$  are the adjoint variables corresponding to  $u$  and  $k$ , respectively, where the indices  $\alpha$ ,  $\beta$ , and  $\gamma$  have been again omitted. The unknown design variables  $\mu$  and  $\rho$  are scalar quantities. Therefore, the inverse metamaterial design problem is defined as

Given  $v_g^m$ , find  $\rho$  and  $\mu$  such that

$$\min L[\rho, \mu, u, k, v, \xi] \quad (20)$$

Various algorithms can be used to solve the minimization problem Eq. (20). For a differentiable  $L$ , gradient-based algorithms are, in general, computationally efficient when compared to gradient-free algorithms. We discuss next the optimality conditions, and a gradient-based approach to resolve the unit cell's properties.

### Optimality Conditions and Adjoint Sensitivity Analysis

We seek a stationary point for  $L$  (20). Equivalently, we seek to satisfy the first-order optimality conditions, which read

$$0 = \delta_v L[\dots](\tilde{v}) \quad \forall \tilde{v} \in \mathcal{V}, \quad 0 = \delta_{\xi} L[\dots](\tilde{\xi}) \quad \forall \tilde{\xi} \in \mathbb{R} \quad (21a)$$

$$0 = \delta_u L[\dots](\tilde{u}) \quad \forall \tilde{u} \in \mathcal{V}, \quad 0 = \delta_k L[\dots](\tilde{k}) \quad \forall \tilde{k} \in \mathbb{C}; \quad \text{and} \quad (21b)$$

$$0 = \delta_{\rho} L[\dots](\tilde{\rho}) \quad \forall \tilde{\rho} \in \mathcal{W}, \quad 0 = \delta_{\mu} L[\dots](\tilde{\mu}) \quad \forall \tilde{\mu} \in \mathcal{W} \quad (21c)$$

We use  $[\dots]$  to abbreviate  $[\rho, \mu, u, k, v, \xi]$  and  $(\tilde{\cdot})$  to denote the direction of the Gâteaux derivative. The function space  $\mathcal{W}$  is defined as

$$\mathcal{W} = \left\{ u \in H^0(\Omega_{\text{cell}}) \mid u(\mathbf{x}) = u \left( \mathbf{x} + \sum_{i=1}^{N_d} m_i \mathbf{p}_i \right) \quad \forall \mathbf{x} \in \partial\Omega_{\text{cell}} \right\} \quad (22)$$

We use an adjoint method to bypass a direct sensitivity analysis, which is, typically, required of any gradient-based algorithm. Accordingly, the first two optimality conditions of Eqs. (21a) and (21b) are first enforced for trial  $\rho$  and  $\mu$ , and then the third optimality condition of Eq. (21c) is used to define the Fréchet derivatives of  $L$  with respect to  $\rho$  and  $\mu$ , denoted by  $g_{\rho}$  and  $g_{\mu}$ , respectively. We note that Eq. (21c) will be satisfied only at the optimum. The detailed expression of the Gâteaux derivatives implicated in the optimality conditions of Eq. (21) are given in Appendix II. Enforcing Eq. (21a) yields the state eigenvalue problem.

Given  $\rho \in \mathcal{W}$ ,  $\mu \in \mathcal{W}$ , and  $\omega \in \mathbb{R}$ , find  $k \in \mathbb{C}$  and  $u \in \mathcal{V} \setminus \{0\}$  such that

$$0 = P(k)(\tilde{v}, u) \quad \forall \tilde{v} \in \mathcal{V} \quad \text{and} \quad (23a)$$

$$0 = \frac{\tilde{\xi}}{2} [a_2(u, u) - 1] \quad \forall \tilde{\xi} \in \mathbb{R} \quad (23b)$$

The enforcement of Eq. (21b) yields the adjoint eigenvalue problem.

Given  $\rho \in \mathcal{W}$ ,  $\mu \in \mathcal{W}$ ,  $\omega \in \mathbb{R}$ ,  $k \in \mathbb{C}$ , and  $u \in \mathcal{V} \setminus \{0\}$ , find  $\xi \in \mathbb{R}$  and  $v \in \mathcal{V}$  such that

$$0 = P(k)(v, \tilde{u}) + \xi a_2(u, \tilde{u}) - \frac{a_1(u, \tilde{u}) + 2\text{Re}\{k\}a_2(u, \tilde{u})}{\omega a_{0,2}(u, u)} (v_g - v_g^m) + \frac{a_1(u, u) + 2\text{Re}\{k\}a_2(u, u)}{\omega [a_{0,2}(u, u)]^2} a_{0,2}(u, \tilde{u}) (v_g - v_g^m) \quad \forall \tilde{u} \in \mathcal{V} \quad \text{and} \quad (24a)$$

$$0 = \tilde{k} a_1(v, u) + 2\tilde{k} k a_2(v, u) - \frac{\tilde{k} a_2(u, u)}{\omega a_{0,2}(u, u)} (v_g - v_g^m) \quad \forall \tilde{k} \in \mathbb{C} \quad (24b)$$

Lastly, given  $\rho \in \mathcal{W}$ ,  $\mu \in \mathcal{W}$ ,  $\omega \in \mathbb{R}$ , the solution of the state eigenvalue problem of Eq. (23) ( $u, k$ ), and the solution of the adjoint eigenvalue problem of Eq. (24) ( $v, \xi$ ), find  $g_{\rho} \in \mathcal{W}$  and  $g_{\mu} \in \mathcal{W}$  such that (Appendix II)

$$\int_{\Omega_{\text{cell}}} \tilde{\rho} g_{\rho} d\Omega = \sum_{\alpha}^{N_{\text{freq}}} \sum_{\beta}^{N_{\text{dir}}} \sum_{\gamma}^{N_{\text{mode}}} \text{Re} \left\{ - \int_{\Omega_{\text{cell}}} \tilde{v} \omega^2 \tilde{\rho} u d\Omega \right\} + \sum_{\alpha}^{N_{\text{freq}}} \sum_{\beta}^{N_{\text{dir}}} \sum_{\gamma}^{N_{\text{mode}}} \text{Re} \left\{ - \left( \frac{\int_{\Omega_{\text{cell}}} i(\text{grad} \tilde{u} \cdot \mu \mathbf{d}u - \mathbf{d}\tilde{u} \cdot \mu \text{grad} u) d\Omega}{2\omega (\int_{\Omega_{\text{cell}}} \tilde{u} \rho u d\Omega)^2} + \frac{2k \int_{\Omega_{\text{cell}}} \tilde{u} \mu u d\Omega}{2\omega (\int_{\Omega_{\text{cell}}} \tilde{u} \rho u d\Omega)^2} \right) \times \left( \int_{\Omega_{\text{cell}}} \tilde{u} \tilde{\rho} u d\Omega \right) (v_g - v_g^m) \right\} \quad \forall \tilde{\rho} \in \mathcal{W} \quad \text{and} \quad (25a)$$

$$\begin{aligned}
\int_{\Omega_{\text{cell}}} \tilde{\mu} g_{\mu} d\Omega &= \sum_{\alpha}^{N_{\text{freq}}} \sum_{\beta}^{N_{\text{dir}}} \sum_{\gamma}^{N_{\text{mode}}} \text{Re} \left\{ k \int_{\Omega_{\text{cell}}} i(\text{grad} \tilde{v} \cdot \tilde{\mu} \mathbf{d}u - \mathbf{d}\tilde{v} \cdot \tilde{\mu} \text{grad} u) d\Omega \right\} \\
&+ \sum_{\alpha}^{N_{\text{freq}}} \sum_{\beta}^{N_{\text{dir}}} \sum_{\gamma}^{N_{\text{mode}}} \text{Re} \left\{ \int_{\Omega_{\text{cell}}} \text{grad} \tilde{v} \cdot \tilde{\mu} \text{grad} u d\Omega \right\} \\
&+ \sum_{\alpha}^{N_{\text{freq}}} \sum_{\beta}^{N_{\text{dir}}} \sum_{\gamma}^{N_{\text{mode}}} \text{Re} \left\{ k^2 \int_{\Omega_{\text{cell}}} \tilde{v} \tilde{\mu} u d\Omega \right\} + \sum_{\alpha}^{N_{\text{freq}}} \sum_{\beta}^{N_{\text{dir}}} \sum_{\gamma}^{N_{\text{mode}}} \text{Re} \left\{ \frac{\xi}{2} \int_{\Omega_{\text{cell}}} \tilde{u} \tilde{\mu} u d\Omega \right\} \\
&+ \sum_{\alpha}^{N_{\text{freq}}} \sum_{\beta}^{N_{\text{dir}}} \sum_{\gamma}^{N_{\text{mode}}} \text{Re} \left\{ \left( \frac{\int_{\Omega_{\text{cell}}} i(\text{grad} \tilde{u} \cdot \tilde{\mu} \mathbf{d}u - \mathbf{d}\tilde{u} \cdot \tilde{\mu} \text{grad} u) d\Omega}{2\omega \int_{\Omega_{\text{cell}}} \tilde{u} \rho u d\Omega} + \frac{2k \int_{\Omega_{\text{cell}}} \tilde{u} \tilde{\mu} u d\Omega}{2\omega \int_{\Omega_{\text{cell}}} \tilde{u} \rho u d\Omega} \right) (v_g - v_g^m) \right\} \quad \forall \tilde{\mu} \in \mathcal{W} \quad (25b)
\end{aligned}$$

Next, armed with the gradients in Eq. (25), we use a conjugate gradient scheme to update the unit cell's properties per the details given in the next session.

### Inversion Process

The stationary point of the Lagrangian is reached only when all of the optimality conditions (21) are satisfied for some distributions of  $\rho$  and  $\mu$ . Otherwise, the properties  $\rho$  and  $\mu$  must be updated at each inversion iteration; the updates can be cast as

$$\rho^{(k+1)} = \rho^{(k)} + \alpha_{\rho}^{(k)} d_{\rho}^{(k)} \quad \text{and} \quad (26a)$$

$$\mu^{(k+1)} = \mu^{(k)} + \alpha_{\mu}^{(k)} d_{\mu}^{(k)} \quad (26b)$$

where  $\rho^{(k+1)}$ ,  $\mu^{(k+1)}$ ,  $\rho^{(k)}$ , and  $\mu^{(k)}$  denote properties at the  $(k+1)$ -th and  $k$ th iterations, respectively;  $d_{\rho}^{(k)}$  and  $d_{\mu}^{(k)}$  are the search directions, and  $\alpha_{\rho}^{(k)}$  and  $\alpha_{\mu}^{(k)}$  are search lengths at the

$k$ th iteration. We use a conjugate gradient method (Fletcher and Reeves 1964; Quarteroni et al. 2010), where

$$d_{\rho}^{(k)} = \begin{cases} -g_{\rho}^{(k)}, & k = 0 \\ -\frac{g_{\rho}^{(k)} \cdot g_{\rho}^{(k)}}{g_{\rho}^{(k-1)} \cdot g_{\rho}^{(k-1)}} g_{\rho}^{(k)}, & k > 0 \end{cases} \quad \text{and}$$

$$d_{\mu}^{(k)} = \begin{cases} -g_{\mu}^{(k)}, & k = 0 \\ -\frac{g_{\mu}^{(k)} \cdot g_{\mu}^{(k)}}{g_{\mu}^{(k-1)} \cdot g_{\mu}^{(k-1)}} g_{\mu}^{(k)}, & k > 0 \end{cases} \quad (27)$$

The search lengths are obtained using the backtracking algorithm (Quarteroni et al. 2010). The updates of Eq. (26) are repeated until trials  $\rho$  and  $\mu$  converge. To make the inversion process robust, we also use a frequency continuation scheme, discussed in the numerical results section. We summarize the inversion process in Algorithm 1.

### Algorithm 1. Inversion process

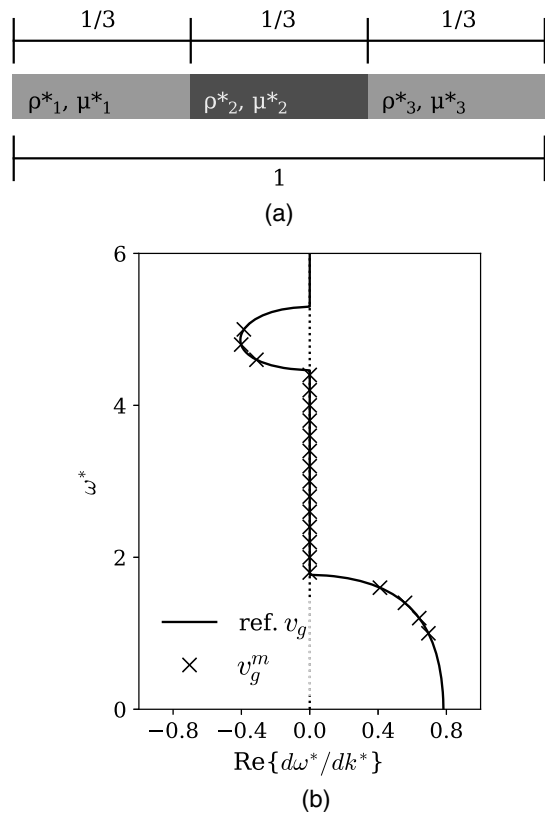
- 1: Sample the target group velocity  $v_g^m$  ( $v_g^m = 0$  for band gaps) at discrete frequencies
- 2: Define the geometry of the unit cell (e.g., periodicity, number of distinct material elements, etc.)
- 3: Set the error tolerance  $\varepsilon$ .
- 4: Initialize the iteration counter  $l \leftarrow 0$
- 5: Set the initial search length
- 6: Set initial guesses for the material properties  $\rho_0$  and  $\mu_0$
- 7: **for**  $\|M_{l+1} - M_l\| > \varepsilon \|M_l\|$  **do**
- 8:   Solve the state eigenvalue problem and evaluate  $M_l$  ▷ Eqs. (16) and (23)
- 9:   Solve the adjoint eigenvalue problem ▷ Eq. (24)
- 10:   Compute the gradient of  $L$  ▷ Eq. (25)
- 11:   Obtain the search direction (e.g., conjugate gradient method)
- 12:   Update the material properties  $\rho_{l+1}$  and  $\mu_{l+1}$  using backtracking algorithm; stop if sufficient-decrease condition is violated
- 13:   Set  $l \leftarrow l + 1$
- 14: **end for**

## Numerical Results

The proposed inverse metamaterial design algorithm was implemented using finite elements in a parallel C code with the aid of PETSc (Balay et al. 2016) and SLEPc (Roman et al. 2016). We describe next one- and two-dimensional examples that help demonstrate the capability and performance of the methodology.

### Unit Cell Design in 1D

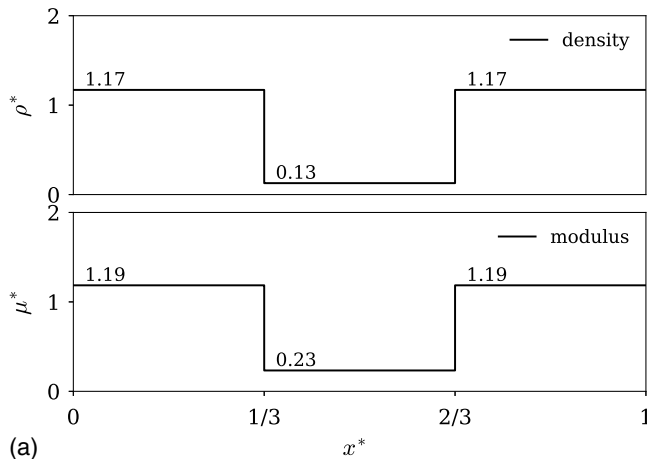
We consider first the case of a 3-material unit cell, whose target group velocity profile is given. The unit cell's topology is fixed, consisting of 3 equal size homogeneous sections with properties  $(\rho_1^*, \mu_1^*)$ ,  $(\rho_2^*, \mu_2^*)$ , and  $(\rho_3^*, \mu_3^*)$  [Fig. 3(a)]. We seek the properties that will result in the given target group velocity profile shown in



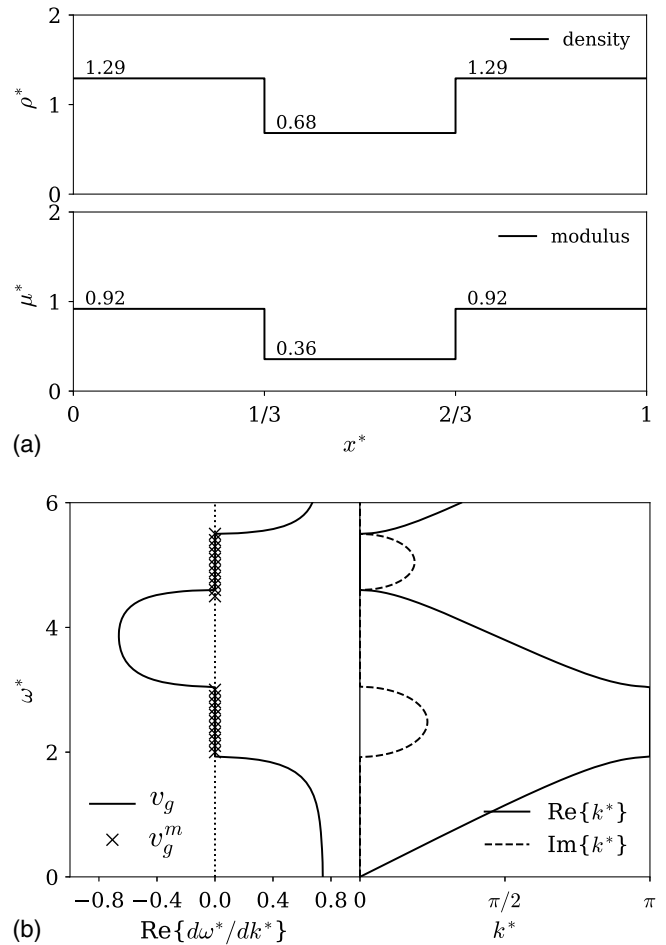
**Fig. 3.** (a) Topology; and (b) target group velocity profile of 1D unit cell design exhibiting a single band gap: solid line shows the synthetic group velocity profile, with crosses (×) marking the sampling points.

Fig. 3(b). The group velocity profile is sampled at 21 points, marked with crosses in Fig. 3(b); notice that the given profile includes a band gap between  $\omega^* = 1.8$  and  $\omega^* = 4.4$ . The inversion process was initiated using near homogeneous properties  $\rho_1^* = \mu_1^* = \rho_3^* = \mu_3^* = 1$  and  $\rho_2^* = \mu_2^* = 0.9$ .

The optimizer resulted in the material distribution shown in Fig. 4(a); Fig. 4(b) depicts the group velocity and band structure of the unit cell using the converged material parameters. As it can be seen, the inversely designed unit cell's velocity profile matches well the target profile.



**Fig. 4.** (a) Inverted properties; and (b) inverted group velocity profile and associated band structure exhibiting a single band gap.



**Fig. 5.** (a) Inverted properties; and (b) inverted group velocity profile and associated band structure exhibiting two band gaps.

Using the same 3-material unit cell topology, we target next a design that ought to exhibit two band gaps, one in the (2, 3) range, and a second one in the (4.5, 5.5) range. We used 22 frequency points to populate the target velocity profile. We start the inversion process with  $\rho_1^* = \mu_1^* = \rho_3^* = \mu_3^* = 1$  and  $\rho_2^* = \mu_2^* = 0.9$ . Fig. 5(a) shows the properties of the converged unit cell, characterized by

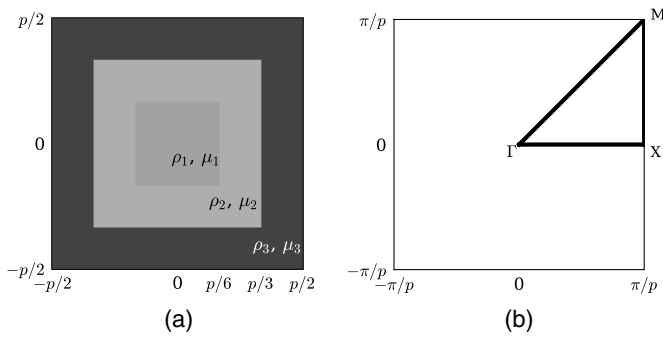


**Fig. 6.** 2D design problem: (a) square unit cell;  $p = 4$  m; and (b) corresponding Brillouin zone and high symmetry lines  $\Gamma - M$ ,  $\Gamma - X$ , and  $X - M$ .

$\rho_1^* = \rho_3^* = 1.29$ ,  $\mu_1^* = \mu_3^* = 0.92$ ,  $\rho_2^* = 0.68$ , and  $\mu_2^* = 0.36$ , while Fig. 5(b) depicts the group velocity profile and associated band structure, where the target band gaps have been very clearly realized.

### Unit Cell Design in 2D

To demonstrate the agility of the method, we consider next the design of a unit cell in two dimensions, where the design goal is for the metamaterial to exhibit an omnidirectional band gap at a prescribed frequency range. Consider the 3-material, 4-m-wide square unit cell depicted in Fig. 6(a); the Brillouin zone is shown in Fig. 6(b). The target band gap is set at  $f \in (4.77, 10.25)$  Hz. The initial guesses are  $\rho_1 = 8,250$  kg/m<sup>3</sup>,  $\mu_1 = 31.99$  MPa,  $\rho_2 = 8,071$  kg/m<sup>3</sup>,  $\mu_2 = 19.72$  MPa,  $\rho_3 = 7,919$  kg/m<sup>3</sup>,  $\mu_3 = 3.06$  MPa;

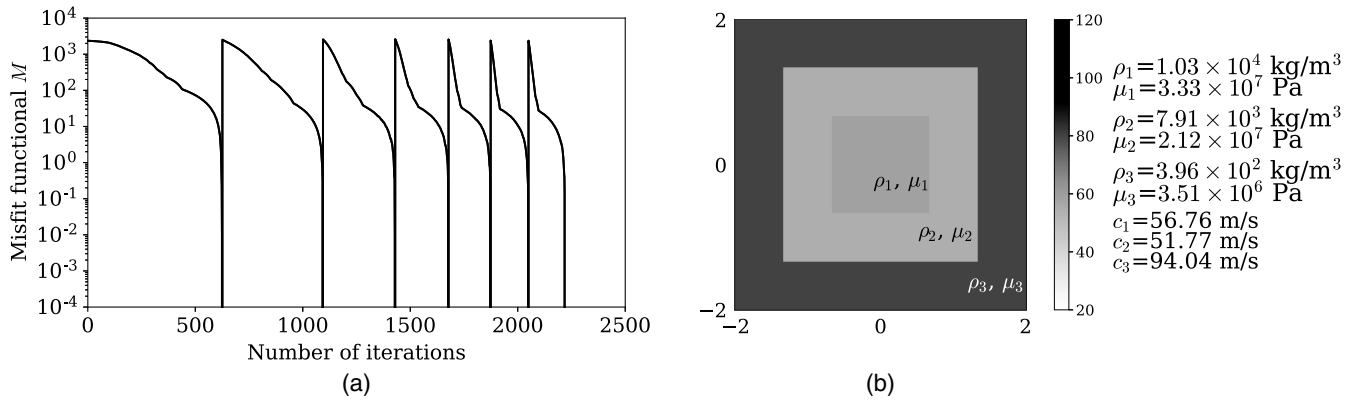


**Fig. 7.** 2D design example of an omnidirectional band gap: (a) misfit functional progression under a 7-stage continuation scheme; and (b) inverted unit cell material profile.

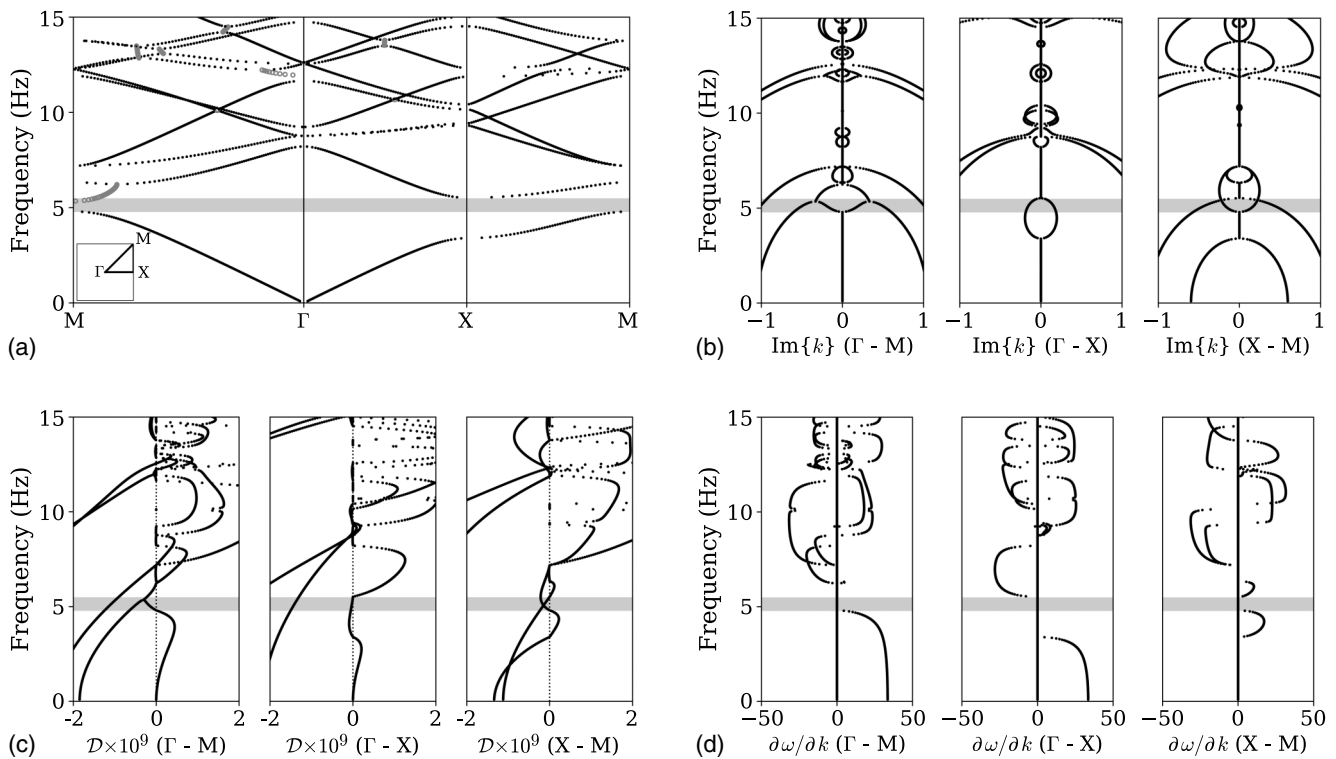


**Fig. 8.** 2D omnidirectional design example: (a) real part of the band structure; (b) imaginary part of the band structure; (c) discriminant; and (d) group velocity, at the end of the first inversion stage.

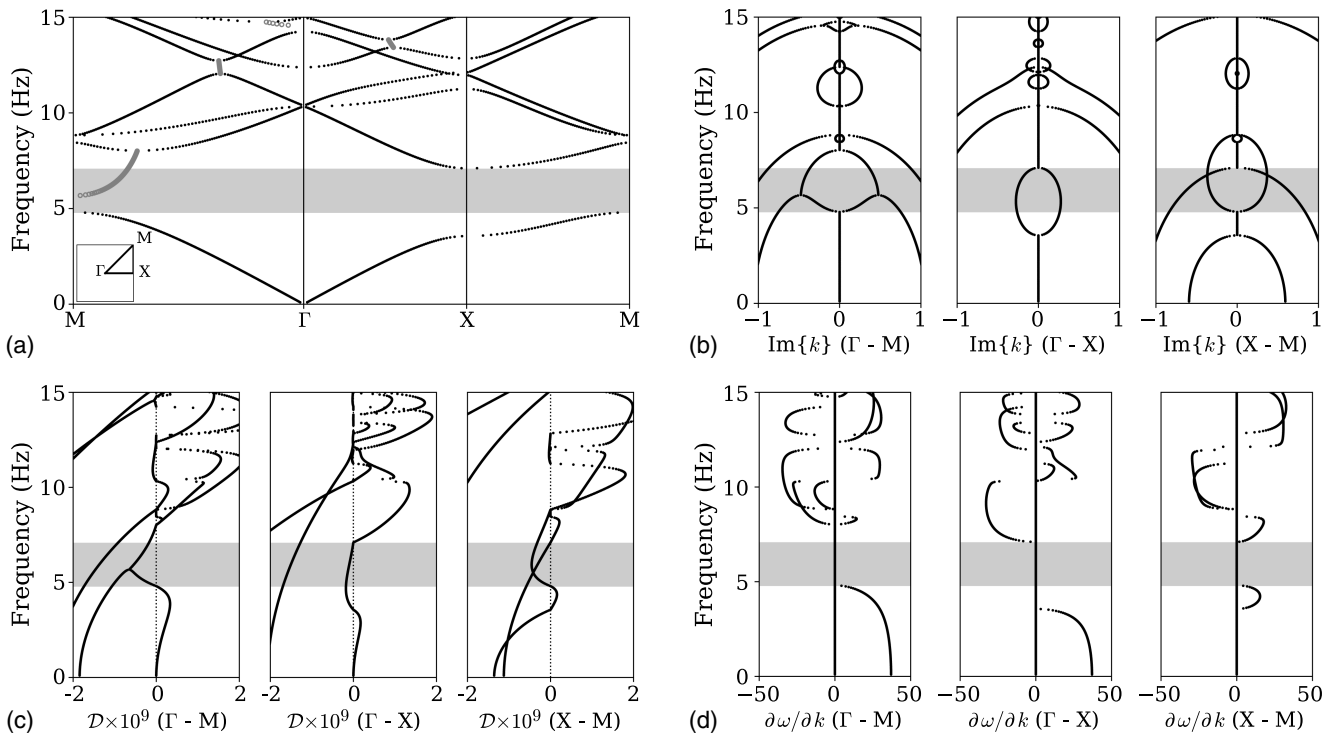


**Fig. 9.** 2D omnidirectional design example: (a) real part of the band structure; (b) imaginary part of the band structure; (c) discriminant; and (d) group velocity, at the end of the third inversion stage.

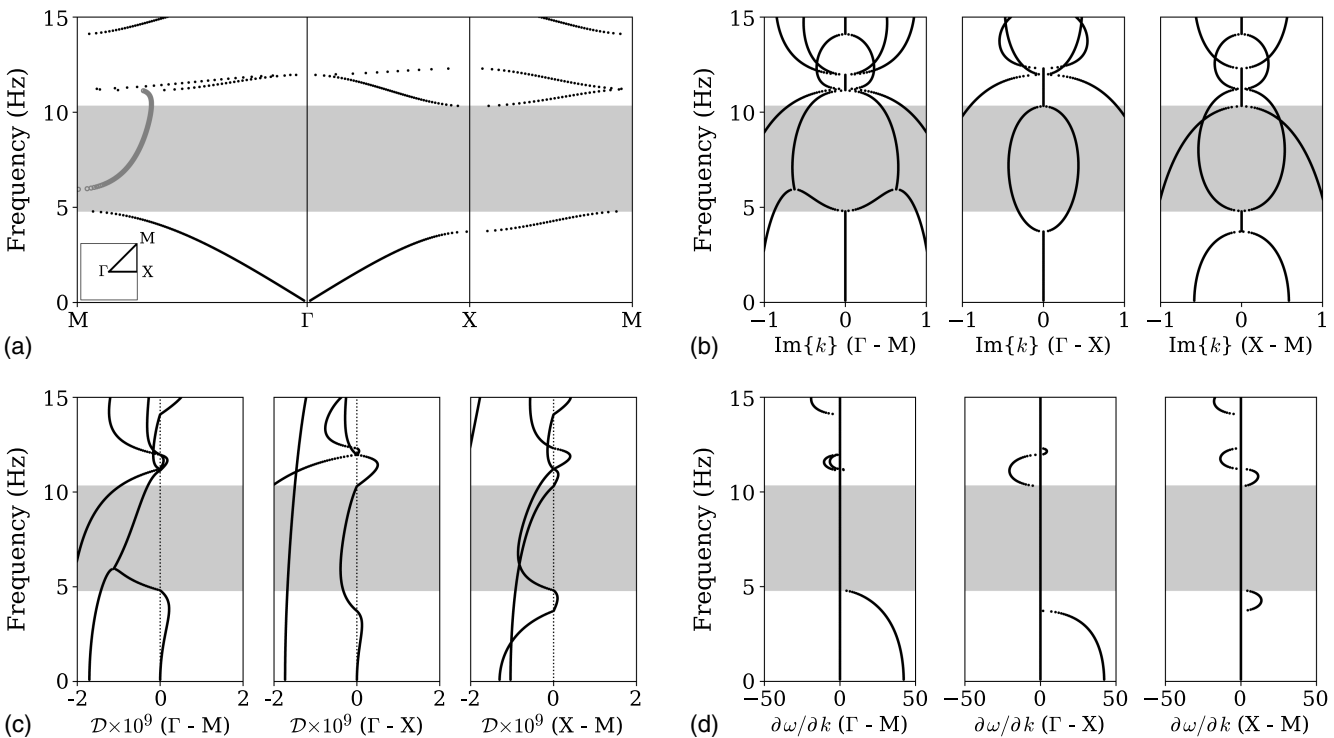


**Fig. 10.** 2D omnidirectional design example: (a) real part of the band structure; (b) imaginary part of the band structure; (c) discriminant; and (d) group velocity, at the end of the final inversion stage.

the initial guesses are informed by a one-dimensional design problem targeting a similar band gap. We use 70 frequency points to mark the band gap ( $N_{\text{freq}} = 70$ ); 2 directions ( $N_{\text{dir}} = 2$ ,  $\mathbf{d}_1 = (1, 0)$  and  $\mathbf{d}_2 = (1/\sqrt{2}, 1/\sqrt{2})$ ); and 3 modes ( $N_{\text{mode}} = 3$ ).

Moreover, we use a staggered process, akin to frequency continuation, where we invert for the cell's properties by first driving the inversion with a portion of the target band gap at (4.77, 5.57) Hz. We then feed the converged material properties as initial guesses for

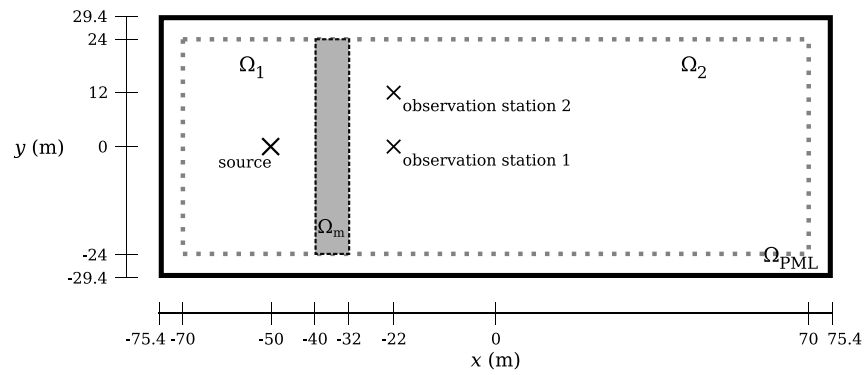


**Fig. 11.** Computational domain for time-domain analyses; the metablock is placed in the shaded region.

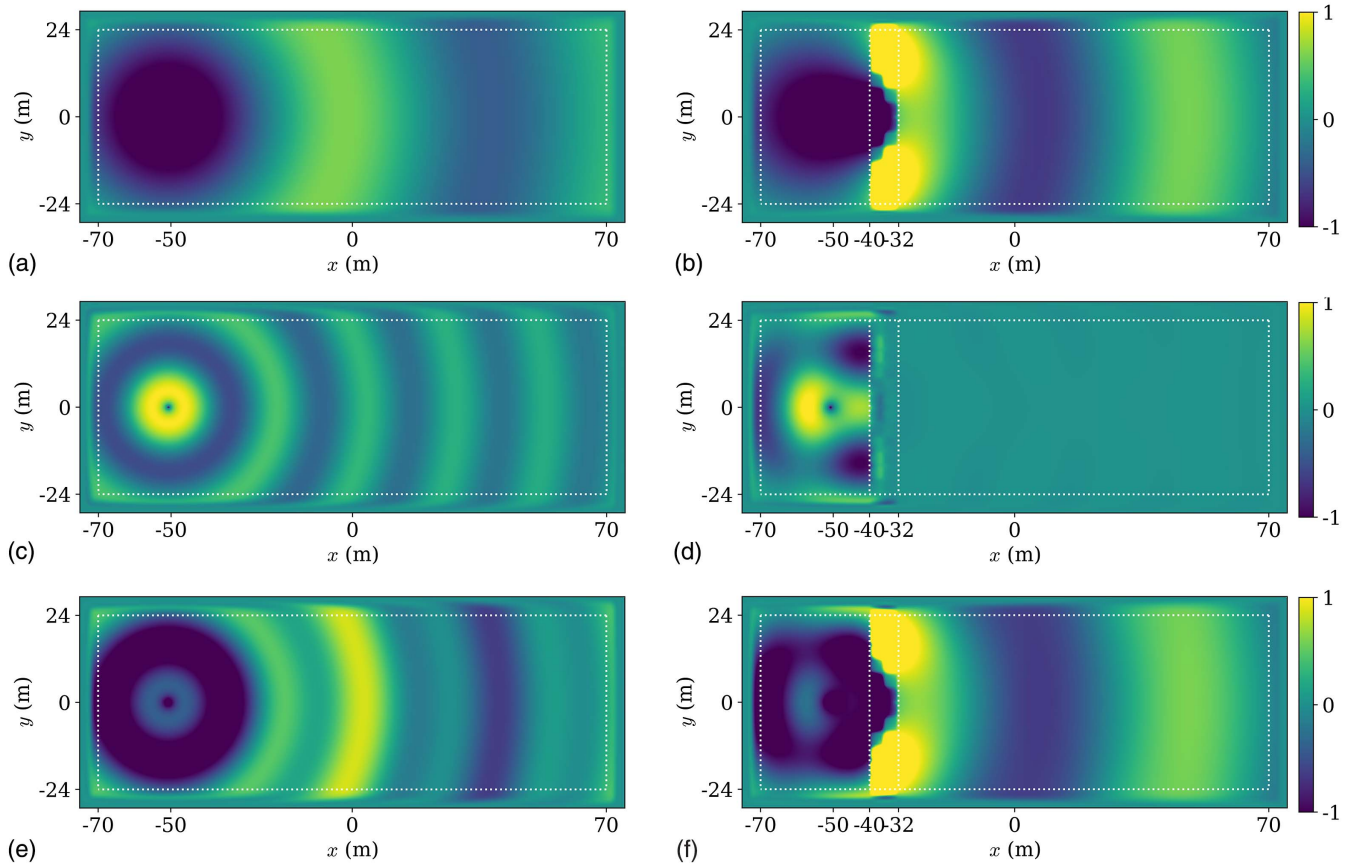
a second stage, where the band gap is now defined between (4.77, 6.37) Hz. We proceed similarly for a total of seven stages by increasing the target range by 0.8 Hz at each stage, until the target band gap is completely covered.

Fig. 7(a) shows the progression of the misfit functional  $M$  with the number of inversion iterations: notice that the end of each stage is marked by a 7-order of magnitude reduction in the misfit. Fig. 7(b) shows the unit cell's inverted properties, while Fig. 8 shows the associated band structure, discriminant, and group velocity at the end of the first stage: a narrow band gap can be observed at the target range of the first stage, i.e., at (4.77, 5.57) Hz. Fig. 9 shows the band structure, discriminant, and the group velocity

at the end of the third stage: notice that, now, a wider band gap is achieved at the target range of the third stage, i.e., at  $f \in (4.77, 7.16)$  Hz, as intended. The band gap after the final stage is completed, is shown in Fig. 10: as it can be seen the target omnidirectional band gap has been successfully attained at  $f \in (4.77, 10.35)$  Hz.

### Time-Domain Analyses

The 2D unit cell constructed in the preceding section's numerical experiment will perform as theoretically expected under ideal conditions of periodicity. However, in practice, a metamaterial can be



**Fig. 12.** Snapshots at  $t = 4$  s of a wavefield induced by monochromatic and dichromatic sources: (a) monochromatic source at  $f_1 = 2.5$  Hz without metablock; (b) monochromatic source at  $f_1 = 2.5$  Hz with metablock; (c) monochromatic source at  $f_2 = 8$  Hz without metablock; (d) monochromatic source at  $f_2 = 8$  Hz with metablock; (e) dichromatic source with  $f_1 = 2.5$  Hz and  $f_2 = 8$  Hz without metablock; and (f) dichromatic source with  $f_1 = 2.5$  Hz and  $f_2 = 8$  Hz with metablock.

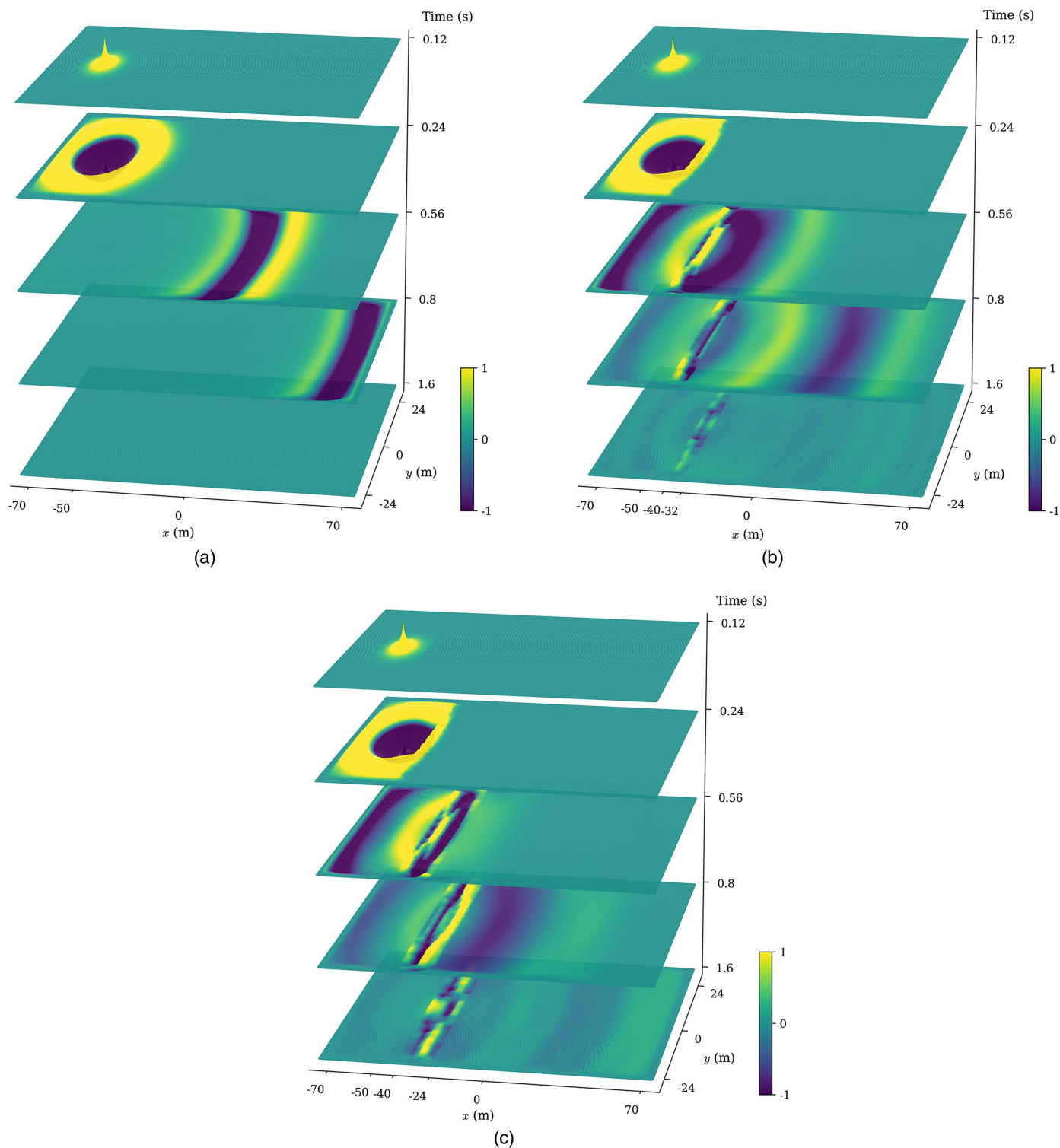


**Fig. 13.** Various snapshots of a wavefield induced by a Ricker pulse with a central frequency of  $f_r = 6$  Hz: (a) homogeneous domain; (b) with a 2 unit-cell-wide metablock at  $x \in (-40, -32)$  m; and (c) with a 4 unit-cell-wide metablock at  $x \in (-40, -24)$  m.

realized only by stacking together a finite number of cells, thereby weakening periodicity. It is then of interest to assess a finite metamaterial block's (henceforth referred to as metablock) performance, especially in the time domain, which is typically the case with the strongest practical interest.

We use the unit cell depicted in Fig. 7(b) to create a metablock that is only two unit cells wide. The metablock occupies  $\Omega_m$  and is embedded within a homogeneous domain  $\Omega$ , as shown in Fig. 11.

With the insertion of  $\Omega_m$ , the homogeneous domain is partitioned into two parts,  $\Omega_1$  and  $\Omega_2$ , such that  $\Omega = \Omega_1 \cup \Omega_2 \cup \Omega_m$ . Moreover, the physical domain  $\Omega$  is surrounded by a buffer of perfectly matched layers (PMLs)  $\Omega_{\text{PML}}$  to simulate wave propagation in an unbounded domain. Then, the computational domain becomes  $\Omega \cup \Omega_{\text{PML}}$ . The material properties of the homogeneous domain  $\Omega_1 \cup \Omega_2$  are  $\rho = 2,000$  kg/m<sup>3</sup> and  $\mu = 80$  MPa; the corresponding wave speed is 200 m/s.

To examine whether an only two-cell-wide metablock is still capable of exhibiting an omnidirectional band gap, we center the 8-m-wide metablock at  $(x, y) = (-36, 0)$  m. A point source is placed at  $(x, y) = (-50, 0)$  m, and two observation stations are set at  $(x, y) = (-22, 0)$  m and  $(-22, 12)$  m, respectively. Two types of sources are used: monochromatic and a narrow-band Ricker pulse. To numerically simulate wave propagation within the heterogeneous metablock  $\Omega_m$ , its homogeneous host  $\Omega_1 \cup \Omega_2$ , and the surrounding buffer  $\Omega_{PML}$ , we use a symmetric mixed-field PML formulation, serendipity isoparametric finite elements, and a Newmark method for time integration; the details can be found in Kucukcoban and Kallivokas (2013).

### Monochromatic Sources

To demonstrate the band-gap behavior of the metablock, we consider first two monochromatic sources:  $p_i^1$  and  $p_i^2$  driven at  $f_1 = 2.5$  Hz and  $f_2 = 8$  Hz, respectively, where

$$p_i^1 = \sin(2\pi f_i t), i = 1 \text{ or } 2 \quad (28)$$

Recall that the frequency  $f_1 = 2.5$  Hz is below the design band gap, while  $f_2 = 8$  Hz is within the design band gap (Fig. 10). The first column of Fig. 12 shows snapshots, taken at  $t = 4$  s, of

the wavefields resulting from  $p_i^1$  for a homogeneous medium, i.e., in the absence of the metablock, whereas the second column of Fig. 12 depicts the wavefields generated in the presence of the metablock. As designed, and despite the small number of cells, the metablock allows the propagation of the 2.5-Hz wave [Figs. 12(a and b)], while arresting the propagation of the 8 Hz wave [Figs. 12(c and d)]. The third row of Fig. 12 shows the effect of the metablock on a dichromatic source driven by both frequencies (it is, effectively, the superposition of the two individual wavefields). It is noteworthy that the metablock's width (8 m) is smaller than one-third of the shortest wavelength (25 m), which alludes to the metablock's subwavelength performance.

### Ricker Pulse—Metablock Width Effect

Next, the same domain is excited using a source with a continuous narrow-band spectrum; specifically, we use a Ricker pulse with a central frequency of  $f_r = 6$  Hz, or  $\omega_r = 2\pi \cdot 6$  rad/s, defined as

$$p_i^r = \frac{(0.25q^2 - 0.5)e^{0.25q^2} - 13e^{-13.5}}{0.5 + 13e^{-13.5}}, \quad 0 \leq t \leq \frac{6\sqrt{6}}{\omega_r} \quad (29)$$

where  $q = \omega_r t - 3\sqrt{6}$ . Fig. 13(a) shows the time evolution of the wavefield in a homogeneous domain (no metablock), for reference.

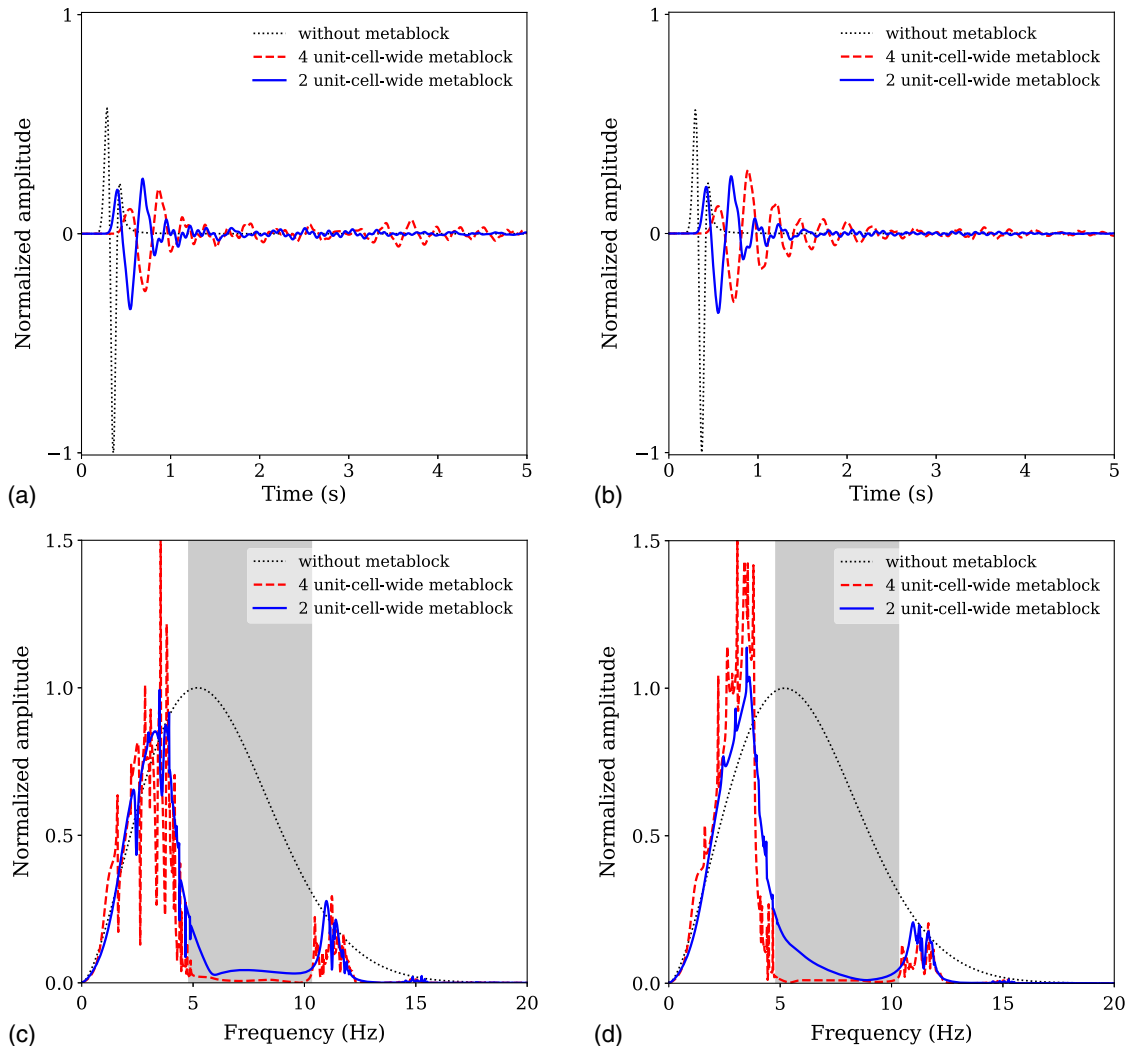


**Fig. 14.** Time traces at two observation stations and corresponding DFTs due to a Ricker pulse with  $f_r = 6$  Hz; the target band gap is shaded in gray: (a) time trace at station 1  $(-22, 0)$  m; (b) time trace at station 2  $(-22, 12)$  m; (c) DFT at station 1  $(-22, 0)$  m; and (d) DFT at station 2  $(-22, 12)$  m.

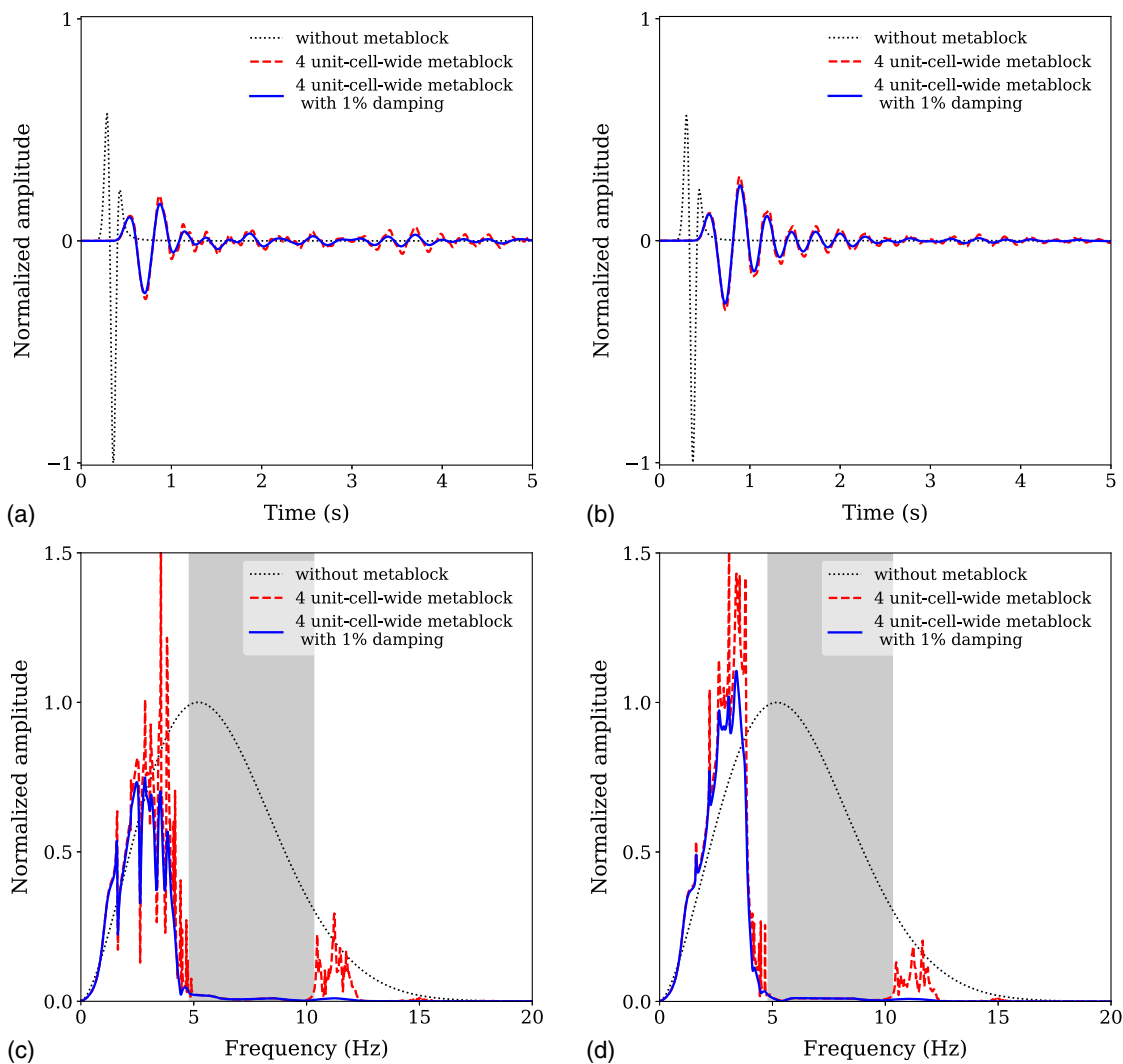


**Fig. 15.** Time traces at two observation stations and corresponding DFTs due to a Ricker pulse with  $f_r = 6$  Hz; comparison of a lossless and lossy (1%) metablock; target band gap is shaded in gray: (a) time trace at station 1  $(-22, 0)$  m; (b) time trace at station 2  $(-22, 12)$  m; (c) DFT at station 1  $(-22, 0)$  m; and (d) DFT at station 2  $(-22, 12)$  m.

First, we compare the response when using metablocks of different widths: a 2-unit-cell-wide and a 4-unit-cell-wide metablock. Figs. 13(b and c) shows snapshots of the associated wavefields. Visually, it can be verified that low frequencies (below the band gap) pass undisturbed through the metablock in both cases. For a more detailed analysis, we use the time-domain response at the two observations stations.

Specifically, Figs. 14(a and b) compare the time traces with and without the metablocks: clearly, the 4-unit-cell-wide metablock's response shows a smoother response. The DFTs shown in Figs. 14(c and d) are more revealing: the presence of the design band gap between 4.77 and 10.35 Hz is evident at both stations, suggesting also the omnidirectionality feature of the metablock. Notice also that there is amplification (compared to the homogeneous case) at frequencies at the edges of the band gap, with stronger amplification at frequencies to the left than to the right of the band gap. If the amplification effect is undesirable, then the insertion of small material damping in the unit cell could alleviate the response, without affecting the band gap (alternatively, the damping can also become part of the inversion problem). To demonstrate the effect, we introduce only in the metablock a 1%

proportional damping (Chopra 2011) at  $f = 2.5$  Hz. The resulting effect is shown in the time traces and the associated DFT of Fig. 15, where the amplification below the band gap has been reduced, with no appreciable effect on the band gap itself.

## Conclusions

We proposed a systematic and general framework to design a unit cell of a periodic medium when given a user-defined target group velocity profile. The method can readily accommodate designing unit cells exhibiting one or more target band gaps. The inverse design metamaterial problem was cast as a dispersion-constrained optimization problem, which was then solved by enlisting an adjoint approach. We demonstrated the method with numerical results in one and two dimensions, including a problem involving the design of a two-dimensional unit cell exhibiting an omnidirectional band gap. We also demonstrated the performance of the inversely designed metamaterials with numerical simulations in the time domain. The methodology is general and can be extended to three dimensions as well as to the case of vector waves.

## Appendix I. Group Velocity and Band Gap

We show that the vanishing of the group velocity at band gaps, i.e., that  $\mathbf{v}_g \cdot \mathbf{d} = 0$  is equivalent to the negativity of the discriminant  $\mathcal{D} < 0$  defined in Eq. (8). Taking the imaginary part of Eq. (5), when  $v$  is replaced by  $u$ , results in

$$0 = \text{Im}\{P(k)(u, u)\} = \text{Im}\{k\}a_1(u, u) + 2\text{Re}\{k\}\text{Im}\{k\}a_2(u, u) = \text{Im}\{k\}[a_1(u, u) + 2\text{Re}\{k\}a_2(u, u)] \quad (30)$$

When  $\mathcal{D} < 0$ , then and only then is  $\text{Im}\{k\} \neq 0$ , and from the foregoing equation it must then also hold that

$$0 = a_1(u, u) + 2\text{Re}\{k\}a_2(u, u) \quad (31)$$

which is the numerator of the group velocity in the direction  $\mathbf{d}$  in Eq. (13); qed.

## Appendix II. Gâteaux Derivatives of $L$

The Fréchet derivative  $g_u$ , or the gradient of  $L$ , is defined as (Stone and Goldbart 2009)

$$\int_{\Omega_{\text{cell}}} \tilde{u} g_u d\Omega = \delta_u L[u](\tilde{u}) \quad (32)$$

where the Gâteaux derivative  $\delta_u L$  is defined as

$$\delta_u L[u](\tilde{u}) = \left. \frac{d}{d\varepsilon} \right|_{\varepsilon=0} L[u + \varepsilon\tilde{u}] \quad (33)$$

The Gâteaux derivatives with respect to the adjoint variables are

$$\delta_v L[\dots](\tilde{v}) = \text{Re}\{P(k)(\tilde{v}, u)\} \quad \text{and} \quad (34a)$$

$$\delta_\xi L[\dots](\tilde{\xi}) = \frac{\tilde{\xi}}{2}[a_2(u, u) - 1] = \text{Re}\left\{\frac{\tilde{\xi}}{2}[a_2(u, u) - 1]\right\} \quad (34b)$$

The Gâteaux derivatives with respect to the state variables are

$$\delta_u L[\dots](\tilde{u}) = \delta_u M[\dots](\tilde{u}) + \delta_u E[\dots](\tilde{u}) \quad \text{and} \quad (35a)$$

$$\delta_k L[\dots](\tilde{k}) = \delta_k M[\dots](\tilde{k}) + \delta_k E[\dots](\tilde{k}) \quad (35b)$$

where

$$\begin{aligned} \delta_u M[\dots](\tilde{u}) &= \text{Re}\left\{-\frac{\text{Re}\{a_1(u, \tilde{u})\} + 2k\text{Re}\{a_2(u, \tilde{u})\}}{\omega a_{0,2}(u, u)}\right\}(v_g - v_g^m) + \text{Re}\left\{\frac{a_1(u, u) + 2ka_2(u, u)}{\omega[a_{0,2}(u, u)]^2} \text{Re}\{a_{0,2}(u, \tilde{u})\}\right\}(v_g - v_g^m) \\ &= \text{Re}\left\{-\frac{a_1(u, \tilde{u}) + 2\text{Re}\{k\}a_2(u, \tilde{u})}{\omega a_{0,2}(u, u)}(v_g - v_g^m)\right\} + \text{Re}\left\{\frac{a_1(u, u) + 2\text{Re}\{k\}a_2(u, u)}{\omega[a_{0,2}(u, u)]^2} a_{0,2}(u, \tilde{u})(v_g - v_g^m)\right\} \end{aligned} \quad (36a)$$

$$\delta_k M[\dots](\tilde{k}) = \text{Re}\left\{-\frac{\tilde{k}a_2(u, u)}{\omega a_{0,2}(u, u)}\right\}(v_g - v_g^m) = \text{Re}\left\{-\frac{\tilde{k}a_2(u, u)}{\omega a_{0,2}(u, u)}(v_g - v_g^m)\right\} \quad (36b)$$

$$\delta_u E[\dots](\tilde{u}) = \text{Re}\{P(k)(v, \tilde{u})\} + \text{Re}\{\xi a_2(u, \tilde{u})\}, \quad \text{and} \quad (36c)$$

$$\delta_k E[\dots](\tilde{k}) = \text{Re}\{\tilde{k}a_1(v, u) + 2k\tilde{k}a_2(v, u)\} \quad (36d)$$

The Gâteaux derivatives with respect to the design variables are

$$\delta_\rho L[\dots](\tilde{\rho}) = \delta_\rho M[\dots](\tilde{\rho}) + \delta_\rho E[\dots](\tilde{\rho}) \quad \text{and} \quad (37a)$$

$$\delta_\mu L[\dots](\tilde{\mu}) = \delta_\mu M[\dots](\tilde{\mu}) + \delta_\mu E[\dots](\tilde{\mu}) \quad (37b)$$

where

$$\delta_\rho M[\dots](\tilde{\rho}) = \sum_{\alpha}^{N_{\text{freq}}} \sum_{\beta}^{N_{\text{dir}}} \sum_{\gamma}^{N_{\text{mode}}} \text{Re}\left\{-\left(\frac{\int_{\Omega_{\text{cell}}} i(\text{grad}\tilde{u} \cdot \mu \mathbf{d}u - \mathbf{d}\tilde{u} \cdot \mu \text{grad}u)d\Omega}{2\omega(\int_{\Omega_{\text{cell}}} \tilde{u} \rho u d\Omega)^2} + \frac{2k \int_{\Omega_{\text{cell}}} \tilde{u} \mu u d\Omega}{2\omega(\int_{\Omega_{\text{cell}}} \tilde{u} \rho u d\Omega)^2}\right)\left(\int_{\Omega_{\text{cell}}} \tilde{u} \tilde{\rho} u d\Omega\right)(v_g - v_g^m)\right\} \quad (38a)$$

$$\delta_{\mu}M[\dots](\tilde{\mu}) = \sum_{\alpha}^{N_{\text{freq}}} \sum_{\beta}^{N_{\text{dir}}} \sum_{\gamma}^{N_{\text{mode}}} \text{Re} \left\{ \left( \frac{\int_{\Omega_{\text{cell}}} i(\text{grad} \tilde{u} \cdot \tilde{\mu} \mathbf{d}u - \mathbf{d}\tilde{u} \cdot \tilde{\mu} \text{grad} u) d\Omega}{2\omega \int_{\Omega_{\text{cell}}} \tilde{u} \rho u d\Omega} + \frac{2k \int_{\Omega_{\text{cell}}} \tilde{u} \tilde{\mu} u d\Omega}{2\omega \int_{\Omega_{\text{cell}}} \tilde{u} \rho u d\Omega} \right) (v_g - v_g^m) \right\} \quad (38b)$$

$$\delta_{\rho}E[\dots](\tilde{\rho}) = \sum_{\alpha}^{N_{\text{freq}}} \sum_{\beta}^{N_{\text{dir}}} \sum_{\gamma}^{N_{\text{mode}}} \text{Re} \left\{ - \int_{\Omega_{\text{cell}}} \tilde{v} \omega^2 \tilde{\rho} u d\Omega \right\}, \quad \text{and} \quad (38c)$$

$$\begin{aligned} \delta_{\mu}E[\dots](\tilde{\mu}) = & \sum_{\alpha}^{N_{\text{freq}}} \sum_{\beta}^{N_{\text{dir}}} \sum_{\gamma}^{N_{\text{mode}}} \text{Re} \left\{ k \int_{\Omega_{\text{cell}}} i(\text{grad} \tilde{v} \cdot \tilde{\mu} \mathbf{d}u - \mathbf{d}\tilde{v} \cdot \tilde{\mu} \text{grad} u) d\Omega \right\} + \sum_{\alpha}^{N_{\text{freq}}} \sum_{\beta}^{N_{\text{dir}}} \sum_{\gamma}^{N_{\text{mode}}} \text{Re} \left\{ \int_{\Omega_{\text{cell}}} \text{grad} \tilde{v} \cdot \tilde{\mu} \text{grad} u d\Omega \right\} \\ & + \sum_{\alpha}^{N_{\text{freq}}} \sum_{\beta}^{N_{\text{dir}}} \sum_{\gamma}^{N_{\text{mode}}} \text{Re} \left\{ k^2 \int_{\Omega_{\text{cell}}} \tilde{v} \tilde{\mu} u d\Omega \right\} + \sum_{\alpha}^{N_{\text{freq}}} \sum_{\beta}^{N_{\text{dir}}} \sum_{\gamma}^{N_{\text{mode}}} \text{Re} \left\{ \frac{\xi}{2} \int_{\Omega_{\text{cell}}} \tilde{u} \tilde{\mu} u d\Omega \right\} \end{aligned} \quad (38d)$$

## Acknowledgments

We wish to thank Professor Andrea Alù for fruitful discussions, as well as the anonymous reviewers for their constructive comments.

## References

- Alagoz, B. B., and S. Alagoz. 2011. "Towards earthquake shields: A numerical investigation of earthquake shielding with seismic crystals." *Open J. Acoust.* 1 (3): 63–69. <https://doi.org/10.4236/oja.2011.13008>.
- Alù, A., and N. Engheta. 2005. "Achieving transparency with plasmonic and metamaterial coatings." *Phys. Rev. E* 72 (1): 016623. <https://doi.org/10.1103/PhysRevE.72.016623>.
- Ashcroft, N. W. 1976. *Solid state physics*. New York: Holt, Rinehart and Winston.
- Balay, S., et al. 2016. *PETSc users manual*. Rep. No. ANL-95/11-Revision 3.7. Lemont, IL: Argonne National Laboratory.
- Banerjee, B. 2011. *An introduction to metamaterials and waves in composites*. Boca Raton, FL: CRC Press.
- Biros, G., L. F. Kallivokas, and S.-W. Na. 2004. "Distributed parameter control of a 2D acoustic Helmholtz problem on a halfspace." In *Proc., 21st Int. Conf. on Theoretical and Applied Mechanics (ICTAM04)*, edited by W. Gutkowski and T. Kowalewski. Warszawa, Poland: IPPT PAN.
- Brillouin, L. 1946. *Wave propagation in periodic structures: Electric filters and crystal lattices*. New York: McGraw-Hill.
- Brun, M., S. Guenneau, and A. B. Movchan. 2009. "Achieving control of in-plane elastic waves." *Appl. Phys. Lett.* 94 (6): 061903. <https://doi.org/10.1063/1.3068491>.
- Castelló-Lurbe, D., V. Torres-Company, and E. Silvestre. 2014. "Inverse dispersion engineering in silicon waveguides." *J. Opt. Soc. Am. B: Opt. Phys.* 31 (8): 1829–1835. <https://doi.org/10.1364/JOSAB.31.001829>.
- Chopra, A. 2011. *Dynamics of structures: International version*. London: Pearson.
- Climente, A., D. Torrent, and J. Sánchez-Dehesa. 2014. "Gradient index lenses for flexural waves based on thickness variations." *Appl. Phys. Lett.* 105 (6): 064101. <https://doi.org/10.1063/1.4893153>.
- Colombi, A. 2016. "Resonant metalenses for flexural waves in plates." *J. Acoust. Soc. Am.* 140 (5): EL423–EL428. <https://doi.org/10.1121/1.4967179>.
- Colombi, A., D. Colquitt, P. Roux, S. Guenneau, and R. V. Craster. 2016a. "A seismic metamaterial: The resonant metawedge." *Sci. Rep.* 6 (1): 27717. <https://doi.org/10.1038/srep27717>.
- Colombi, A., S. Guenneau, P. Roux, and R. V. Craster. 2016b. "Transformation seismology: Composite soil lenses for steering surface elastic

- Rayleigh waves." *Sci. Rep.* 6 (1): 25320. <https://doi.org/10.1038/srep25320>.
- Dubois, M., M. Farhat, E. Bossy, S. Enoch, S. Guenneau, and P. Sebbah. 2013. "Flat lens for pulse focusing of elastic waves in thin plates." *Appl. Phys. Lett.* 103 (7): 071915. <https://doi.org/10.1063/1.4818716>.
- Fathi, A., L. F. Kallivokas, and B. Poursartip. 2015. "Full-waveform inversion in three-dimensional PML-truncated elastic media." *Comput. Methods Appl. Mech. Eng.* 296 (Nov): 39–72. <https://doi.org/10.1016/j.cma.2015.07.008>.
- Finocchio, G., O. Casablanca, G. Ricciardi, U. Alibrandi, F. Garesci, M. Chiappini, and B. Azzaroni. 2014. "Seismic metamaterials based on isochronous mechanical oscillators." *Appl. Phys. Lett.* 104 (19): 191903. <https://doi.org/10.1063/1.4876961>.
- Fletcher, R., and C. M. Reeves. 1964. "Function minimization by conjugate gradients." *Comput. J.* 7 (2): 149–154. <https://doi.org/10.1093/comjnl/7.2.149>.
- Goh, H., and L. F. Kallivokas. 2019. "Inverse metamaterial design for controlling band gaps in scalar wave problems." *Wave Motion* 88 (May): 85–105. <https://doi.org/10.1016/j.wavemoti.2019.02.001>.
- Huang, J., W. Liu, and Z. Shi. 2017. "Surface-wave attenuation zone of layered periodic structures and feasible application in ground vibration reduction." *Constr. Build. Mater.* 141 (Jun): 1–11. <https://doi.org/10.1016/j.conbuildmat.2017.02.153>.
- Kallivokas, L., A. Fathi, S. Kucukcoban, K. Stokoe, J. Bielak, and O. Ghattas. 2013. "Site characterization using full waveform inversion." *Soil Dyn. Earthquake Eng.* 47 (Apr): 62–82. <https://doi.org/10.1016/j.soildyn.2012.12.012>.
- Krödel, S., N. Thomé, and C. Daraio. 2015. "Wide band-gap seismic meta-structures." *Extreme Mech. Lett.* 4 (Sep): 111–117. <https://doi.org/10.1016/j.eml.2015.05.004>.
- Kucukcoban, S., H. Goh, and L. F. Kallivokas. 2019. "On the full-waveform inversion of lamé parameters in semi-infinite solids in plane strain." *Int. J. Solids Struct.* 164 (Jun): 104–119. <https://doi.org/10.1016/j.ijsolstr.2019.01.019>.
- Kucukcoban, S., and L. Kallivokas. 2013. "A symmetric hybrid formulation for transient wave simulations in PML-truncated heterogeneous media." *Wave Motion* 50 (1): 57–79. <https://doi.org/10.1016/j.wavemoti.2012.06.004>.
- Luo, C., S. G. Johnson, J. D. Joannopoulos, and J. B. Pendry. 2003. "Subwavelength imaging in photonic crystals." *Phys. Rev. B* 68 (4): 045115. <https://doi.org/10.1103/PhysRevB.68.045115>.
- Mashayekh, H., L. F. Kallivokas, and J. L. Tassoulas. 2018. "Parameter estimation in layered media using dispersion-constrained inversion." *J. Eng. Mech.* 144 (11): 04018099. [https://doi.org/10.1061/\(ASCE\)EM.1943-7889.0001527](https://doi.org/10.1061/(ASCE)EM.1943-7889.0001527).
- Meseguer, F., M. Holgado, D. Caballero, N. Benaches, J. Sánchez-Dehesa, C. López, and J. Linares. 1999. "Rayleigh-wave attenuation by a

- semi-infinite two-dimensional elastic-band-gap crystal." *Phys. Rev. B* 59 (19): 12169–12172. <https://doi.org/10.1103/PhysRevB.59.12169>.
- Miniaci, M., A. Krushynska, F. Bosia, and N. M. Pugno. 2016. "Large scale mechanical metamaterials as seismic shields." *New J. Phys.* 18 (8): 083041. <https://doi.org/10.1088/1367-2630/18/8/083041>.
- Moiseyenko, R. P., and V. Laude. 2011. "Material loss influence on the complex band structure and group velocity in phononic crystals." *Phys. Rev. B* 83 (6): 064301. <https://doi.org/10.1103/PhysRevB.83.064301>.
- Movchan, A., N. Movchan, I. Jones, and D. Colquitt. 2018. *Mathematical modeling of waves in multi-scale structured media*. Boca Raton, FL: CRC Press.
- Newton, I. 1740. *The system of the world, demonstrated in an easy and popular manner: Being a proper introduction of the most sublime philosophy*. London: J. Robinson.
- Norris, A. N. 2008. "Acoustic cloaking theory." *Proc. R. Soc. London A* 464 (2097): 2411–2434. <https://doi.org/10.1098/rspa.2008.0076>.
- Palermo, A., S. Krödel, K. H. Matlack, R. Zaccherini, V. K. Dertimanis, E. N. Chatzi, A. Marzani, and C. Daraio. 2018. "Hybridization of guided surface acoustic modes in unconsolidated granular media by a resonant metasurface." *Phys. Rev. Appl.* 9 (5): 054026. <https://doi.org/10.1103/PhysRevApplied.9.054026>.
- Pendry, J. B. 2000. "Negative refraction makes a perfect lens." *Phys. Rev. Lett.* 85 (18): 3966–3969. <https://doi.org/10.1103/PhysRevLett.85.3966>.
- Qian, X., and O. Sigmund. 2011. "Isogeometric shape optimization of photonic crystals via Coons patches." *Comput. Methods Appl. Mech. Eng.* 200 (25): 2237–2255. <https://doi.org/10.1016/j.cma.2011.03.007>.
- Quarteroni, A., R. Sacco, and F. Saleri. 2010. Vol. 37 of *Numerical mathematics*. New York: Springer.
- Rayleigh, L. 1887. "Xvii. On the maintenance of vibrations by forces of double frequency, and on the propagation of waves through a medium endowed with a periodic structure." *London Edinburgh Dublin Philos. Mag. J. Sci.* 24 (147): 145–159. <https://doi.org/10.1080/14786448708628074>.
- Roman, J. E., C. Campos, E. Romero, and A. Tomas. 2016. *SLEPc users manual*. Rep. No. DSIC-II/24/02—Revision 3.7. València, Spain: Departamento de Sistemas Informáticos y Computación, Universitat Politècnica de València.
- Rupp, C. J., A. Evgrafov, K. Maute, and M. L. Dunn. 2007. "Design of phononic materials/structures for surface wave devices using topology optimization." *Struct. Multidiscip. Optim.* 34 (2): 111–121. <https://doi.org/10.1007/s00158-006-0076-0>.
- Sakoda, K. 2004. Vol. 80 of *Optical properties of photonic crystals*. New York: Springer.
- Schurig, D., J. J. Mock, B. J. Justice, S. A. Cummer, J. B. Pendry, A. F. Starr, and D. R. Smith. 2006. "Metamaterial electromagnetic cloak at microwave frequencies." *Science* 314 (5801): 977–980. <https://doi.org/10.1126/science.1133628>.
- Sigmund, O., and J. Søndergaard Jensen. 2003. "Systematic design of phononic band-gap materials and structures by topology optimization." *Philos. Trans. R. Soc. London A* 361 (1806): 1001–1019. <https://doi.org/10.1098/rsta.2003.1177>.
- Stone, M., and P. Goldbart. 2009. *Mathematics for physics: A guided tour for graduate students*. Cambridge: Cambridge University Press.
- Torrent, D., Y. Pennec, and B. Djafari-Rouhani. 2014. "Omnidirectional refractive devices for flexural waves based on graded phononic crystals." *J. Appl. Phys.* 116 (22): 224902. <https://doi.org/10.1063/1.4903972>.
- Wagner, P.-R., V. K. Dertimanis, E. N. Chatzi, and J. L. Beck. 2018. "Robust-to-uncertainties optimal design of seismic metamaterials." *J. Eng. Mech.* 144 (3): 04017181. [https://doi.org/10.1061/\(ASCE\)EM.1943-7889.0001404](https://doi.org/10.1061/(ASCE)EM.1943-7889.0001404).
- Wang, Y., Z. Luo, N. Zhang, and Z. Kang. 2014. "Topological shape optimization of microstructural metamaterials using a level set method." *Comput. Mater. Sci.* 87 ( May): 178–186. <https://doi.org/10.1016/j.commatsci.2014.02.006>.